



# Understanding the alleviation of “Double-ITCZ” bias in CMIP6 models from the perspective of atmospheric energy balance

Zikun Ren<sup>1,2</sup> · Tianjun Zhou<sup>1,2</sup>

Received: 29 December 2023 / Accepted: 6 April 2024  
© The Author(s) 2024

## Abstract

The simulation of tropical precipitation has been a challenge to climate models. The multi-model ensemble mean of CMIP6 models only show limited improvement relative to the CMIP3 and CMIP5 models. However, a simple ensemble mean may mask the improvement of individual models. Here we evaluated 20 CMIP6 models and their corresponding earlier version in CMIP5. The results show that the CMIP6 models is significantly improved in the tropical precipitation compared to their counterparts in CMIP5, and the alleviation of bias mainly happened in the top ten model pairs with largest RMSE reduction (TOP10). For the mean of TOP10, the antisymmetric (symmetric) bias mode in CMIP5 is significantly reduced by 55% (78%). Further energetics evaluation shows that, the CMIP5-to-CMIP6 decrease of antisymmetric bias in the bulk of TOP10 models is accompanied by more realistic southward cross-equatorial atmospheric energy transport ( $AET_{EQ}$ ), which is mainly contributed by the better representation of the extra-tropical surface turbulent flux ( $STF$ ). On the other hand, the decrease in the symmetric bias of TOP10 models is associated with the enlargement of the negative bias in the seasonal contrast of  $AET_{EQ}$ , which is caused by the alleviation of the biases in the seasonal contrast of extra-tropical  $STF$ . Our analysis revealed the improvement in the simulation of tropical precipitation in CMIP6, and we pointed out that the improvement is associated with the model-generational changes in the simulated atmospheric energy balances.

**Keywords** Double-ITCZ problem · CMIP5,6 · Model improvement · Atmospheric energy balance

## 1 Introduction

The ocean–atmosphere coupled general circulation models tend to overestimate oceanic precipitation in the southern tropics and underestimate precipitation in the equatorial Pacific (Lin 2007; Wielicki et al. 1996). This problem is called the “double intertropical convergence zone (ITCZ)”, because the simulated precipitation appears to have another ITCZ-like rainband over the southern deep tropics. Since the bias of “double ITCZ” may influence the creditability of climate models in the projection of future climate change,

resolving the “double ITCZ” has been of great concern to climate modeling community.

Previous studies have pointed out that the zonal mean “double ITCZ” could be separated into the hemispherical antisymmetric and symmetric components (Adam et al. 2016; Kim et al. 2021; Li and Xie 2014). The independence between these two components implied the distinct physical mechanisms controlling them. The antisymmetric component reflects the bias in the location of the annual mean ITCZ, which is typically represented by the centroid of tropical precipitation (Frierson and Hwang 2012), and the symmetric component is associated with the width of tropical precipitation and the seasonal migration of the ITCZ (Donohoe et al. 2019; Kim et al. 2021). Although the alleviation of antisymmetric and symmetric “double ITCZ” from CMIP5 to the CMIP6 is limited for the multi-model ensemble mean (Tian and Dong 2020), the top five models in CMIP6 showed better performance in pattern correlation of southeast Pacific precipitation when compared to CMIP5 (Si et al. 2021). These two contrasting results indicate that the whole ensemble average may mask some potential progresses of individual models, due to the differences in the

---

Zikun Ren is the first contributor of this paper.

---

✉ Tianjun Zhou  
zhoutj@lasg.iap.ac.cn  
Zikun Ren  
renzk@lasg.iap.ac.cn

<sup>1</sup> LASG, Institute of Atmospheric Physics, Chinese Academy of Sciences, Beijing 10029, China

<sup>2</sup> University of Chinese Academy of Sciences, Beijing 100049, China

size and constitution of the whole model ensemble between CMIP5 and CMIP6. Therefore, a comparison between the CMIP5 models and their respective new version in CMIP6 should be helpful to reveal the potential improvements.

The annual mean locations of the ITCZ in the coupled models are tightly associated with the cross-equatorial energy transport (Hwang and Frierson 2013; Loeb et al. 2016). Multiple processes are reported to contribute to this energetics bias, including the improper representation of convection and cloud in the tropics (Bellucci et al. 2010; Xiang et al. 2017; Zhang and Wang 2006; Zhou et al. 2022), shortwave radiation bias in the Southern Ocean (Hwang and Frierson 2013; Kawai et al. 2021; Mechoso et al. 2016), and the land surface temperature (Zhou and Xie 2017). From a perspective of hemispheric energy balance, Loeb et al. (2016) applied an energetics framework to evaluate energy budget governing the antisymmetric “double ITCZ” problem. This framework incorporated the radiation and surface turbulent heat fluxes in the observational constraint to establish a closed observational energy balance. By decomposing the cross-equatorial energy transport, this framework provided a practical approach to identify whether the improvement in the cross-equatorial energy transport results from solid progress or from compensation between different biases in the energy budget.

In contrast to the anti-symmetric component of “double ITCZ”, the symmetric “double ITCZ” bias is associated with the annual cycle of the cross-equatorial atmospheric energy transport (Donohoe et al. 2019; Kim et al. 2021) and the annual mean net energy input to the atmosphere near the equator (Adam et al. 2016; Bischoff and Schneider 2016; Kim et al. 2021). Among the constitutions of the seasonal cross-equatorial atmospheric energy transport, the inter-hemispheric contrast of the clear-sky atmospheric shortwave absorption is significantly correlated to the index of symmetric “double ITCZ”, which implies that the differences in radiative transfer parameterizations may lead to the inter-model spread of symmetric ITCZ bias (Kim et al. 2021). In addition, the symmetric component of “double ITCZ” bias is also reported to be closely linked to a “cold tongue” over the equatorial Pacific (Kim et al. 2021; Li and Xie 2014; Ma et al. 2023; Wang et al. 2020). Therefore, in some previous work, the symmetric “double ITCZ” is also investigated in relation to “cold tongue” problem to distinguish it from the antisymmetric “double ITCZ” problem (Li et al. 2015a; Li and Xie 2014). Within the framework of atmospheric energetics framework, the equatorial “cold tongue” is reported to bias precipitation by the abnormal surface energy flux near the equator (Kim et al. 2021). The surface energy flux near the equator contributes to the bias in the net energy input to the atmosphere near the equator and leads to the symmetric “double ITCZ” (Kim et al. 2021). However, these previous works on the physical processes underlying the symmetric component of “double ITCZ” biases were mainly based on

inter-model correlation analysis, a quantitative evaluation with a closed hemispheric energetic budget framework is lacking for the CMIP models.

In this study, we aim to answer the following questions: (1) Do the antisymmetric and symmetric components of “double ITCZ” biases in CMIP6 models exhibit improvements compared with their earlier version in CMIP5? (2) Which energy processes in the hemispheric energy balance lead to improvements in the CMIP6 models?

The remainder of the paper is organized as follows. In Sect. 2, we describe the data and the used approaches. In Sect. 3, we exhibit the primary results of this study followed by a summary in Sect. 4.

## 2 Data and methods

### 2.1 Observations and model simulations

To represent the observed atmospheric energy balance, the satellite-derived radiative fluxes products and atmospheric reanalysis are combined to supply a closed climatology of energy budget. The following data are used in our analysis:

- 1) Radiative fluxes data are from the Clouds and the Earth’s Radiant Energy System (CERES) Energy Balanced and Filled (EBAF) Ed4.1 product for the TOA (Loeb et al. 2018) and surface (Kato et al. 2018).
- 2) Total atmospheric energy divergence and tendency for January 2005–December 2015 is obtained from the mass corrected vertically integrated energy budget terms (Mayer et al. 2021) for ERA5 (Hersbach et al. 2020) data. All these patterns of atmospheric energy balance are regridded to  $2.5^\circ \times 2.5^\circ$  by using the second-order conservative interpolation (Jones 1999).

Monthly precipitation rates from the Global Precipitation Climatology Project (GPCP) (Adler et al. 2003) version 2.2 and Climate Prediction Center (CPC) merged analysis precipitation (CMAP) version 12.01 product (Xie and Arkin 1997) are also used in this study to characterize the observed precipitation. Both datasets rely on satellite observations and rain gauge data with a spatial resolution of  $2.5^\circ \times 2.5^\circ$  spanning from 1979 to present day. We employ both GPCP and CMAP to represent the uncertainty in observations.

The monthly output of precipitation, radiation fluxes, air temperature, geopotential height, specific humidity, near-surface air temperature, and near-surface specific humidity from the historical experiment of 20 CMIP5 (Taylor et al. 2012) models and their respective updated versions in CMIP6 (Eyring et al. 2016) are analyzed (Table 1). Only the first realization of each model is analyzed. All the data are regridded to  $2.5^\circ \times 2.5^\circ$  by using second-order conservative

**Table 1** The information of the 20 CMIP5 and CMIP6 models used in this study

CMIP6 Models	CMIP5 Models	Institute/Country
ACCESS-CM2	ACCESS1-3	CSIRO/Australian
BCC-CSM2-MR	bcc-csm1-1-m	BCC-CMA/China
BCC-ESM1	bcc-csm1-1	BCC-CMA/China
CanESM5	CanESM2	CCCMA/Canada
CESM2	CESM1-CAM5	NCAR/USA
CESM2-WACCM	CESM1-WACCM	NCAR/USA
CMCC-ESM2	CMCC-CESM	CMCC/Italy
CNRM-CM6-1	CNRM-CM5	CNRM-CERFACS/France
FGOALS-f3-L	FGOALS-s2	LASG-IAP/China
FGOALS-g3	FGOALS-g2	LASG-IAP/China
GFDL-CM4	GFDL-CM3	GFDL-NOAA/USA
GFDL-ESM4	GFDL-ESM2M	GFDL-NOAA/USA
GISS-E2-1-G	GISS-E2-R	GISS-NASA/USA
GISS-E2-1-H	GISS-E2-H	GISS-NASA/USA
INM-CM5-0	inmcm4	INM/Russia
IPSL-CM6A-LR	IPSL-CM5A-LR	IPSL/France
MIROC6	MIROC5	MIROC/Japan
MRI-ESM2-0	MRI-ESM1	MRI/Japan
NorESM2-LM	NorESM1-M	NCC/Norway
UKESM1-0-LL	HadGEM2-ES	MOHC/UK

interpolation (Jones 1999). To highlight the biases in the spatial distribution of tropical precipitation, the tropical mean precipitation simulated by each model has been scaled to the GPCP observation before further analysis. This scaling approach is formulated as below:

$$P_{scaled} = P_{SIM} \cdot \frac{\overline{P_{OBS}}}{\overline{P_{SIM}}}, \tag{1}$$

where  $P_{scaled}$  is the scaled precipitation,  $P_{SIM}$  is the precipitation simulated by the models,  $P_{OBS}$  is the observed precipitation, and the overbar \* indicates the tropical spatial mean. This scaling is equivalent to the normalization of tropical precipitation (Kim et al. 2021; Li and Xie 2014), but keeps the magnitude and unit of precipitation.

### 2.2 Definition of two sub-ensemble

To identify some potential improvement in individual models from CMIP5 to CMIP6, we defined the top ten model ensemble (TOP10) and bottom ten model ensemble (BOT10) of CMIP5 (CMIP6) and contrasted them with the multi-model ensemble (MME) of all the 20 models used in this work. The TOP10 of CMIP5 (CMIP6) is defined as the ensemble of the ten CMIP5 (CMIP6) models with largest reduction in the spatial root mean square error (RMSE) of the tropical precipitation from CMIP5 to CMIP6, while the

BOT10 contains other ten models in the CMIP5 (CMIP6). Table 2 shows the RMSE of these models and their RMSE changes from CMIP5 to CMIP6.

### 2.3 Method for identifying the leading modes of the “double ITCZ” biases

To clearly separate the symmetric and anti-symmetric components of spread, the scaled zonal mean tropical precipitation biases of CMIP5 and CMIP6 models are decomposed into the antisymmetric and symmetric components. The formula of this decomposition is as follows,

$$F(\theta) = A(\theta) + S(\theta), \tag{2}$$

where  $F(\theta)$  is the zonal mean bias field,  $\theta$  represent the latitude;  $S(\theta) = (F(\theta) + F(-\theta))/2$ , which is the symmetric component of the  $F(\theta)$ ;  $A(\theta) = F(\theta) - S(\theta)$ , which represents the antisymmetric component. It can be demonstrated that:

$$\int_{-\frac{\pi}{6}}^{\frac{\pi}{6}} S(\theta) \times A(\theta) d\theta = 0 \tag{3}$$

where  $\theta$  represent the latitude. Therefore, the tropical integral of the mean square of the CMIP6 biases can be equivalently separated into antisymmetric and symmetric components:

$$\int_{-\frac{\pi}{6}}^{\frac{\pi}{6}} \frac{\sum_{i=1}^n F_i(\theta)^2}{n} d\theta = \int_{-\frac{\pi}{6}}^{\frac{\pi}{6}} \frac{\sum_{i=1}^n A_i(\theta)^2}{n} d\theta + \int_{-\frac{\pi}{6}}^{\frac{\pi}{6}} \frac{\sum_{i=1}^n S_i(\theta)^2}{n} d\theta. \tag{4}$$

where  $n = 40$  is the number of the models we used. Note that, different with Kim et al. (2021), our decomposition here is applied to the biases relative with the GPCP observation, rather than to the inter-model spread.

On the basis of this decomposition, we respectively performed an EOF analysis on the antisymmetric and symmetric parts of the biases among the 40 models to identify the leading modes of the “double ITCZ” biases. Traditional inter-model EOF analysis always removed the multi-model ensemble mean to characterize the inter-model spread (Kim et al. 2021; Li and Xie 2012, 2014). Since our objective here is to quantify the model biases with respect to observations, the MME biases are retained in our EOF analysis. As a result, the absolute value of the principal components (PCs) from these EOF analyses could reflect the amplitude of each model’s biases. The sign of each PCs determines the sign of the corresponding EOF pattern of the biases.

### 2.4 Atmospheric energy balance

The inter-hemispheric asymmetry and the width of the simulated tropical precipitation are respectively determined by the

**Table 2** The tropical precipitation RMSE of the 20 pairs of CMIP5 and CMIP6 models and their changes from CMIP5 to CMIP6. The names and RMSEs of CMIP6 models are in the brackets. Model pairs are ordered according to the RMSE changes from CMIP5 to CMIP6 (from negative to positive). The bold text denotes the TOP10 models

CMIP5(CMIP6) Model Pairs	RMSE of CMIP5(CMIP6) Models (units: $\text{mmday}^{-1}$ )	RMSE change from CMIP5 to CMIP6 (units: $\text{mmday}^{-1}$ )
GFDL-CM3 (GFDL-CM4)	1.638 (1.164)	-0.474
CESM1-WACCM (CESM2-WACCM)	1.433(1.082)	-0.351
bcc-csm1-1-m (BCC-CSM2-MR)	1.935(1.585)	-0.35
CMCC-CESM (CMCC-ESM2)	1.709(1.394)	-0.315
CESM1-CAM5 (CESM2)	1.325(1.039)	-0.286
MRI-ESM1 (MRI-ESM2-0)	1.789(1.506)	-0.284
GFDL-ESM2M (GFDL-ESM4)	1.566(1.293)	-0.274
MIROC5 (MIROC6)	1.288(1.068)	-0.221
FGOALS-s2 (FGOALS-f3-L)	1.839(1.641)	-0.198
inmcm4 (INM-CM5-0)	1.841(1.657)	-0.184
IPSL-CM5A-LR (IPSL-CM6A-LR)	1.834(1.651)	-0.183
NorESM1-M (NorESM2-LM)	1.516(1.346)	-0.17
GISS-E2-H (GISS-E2-1-H)	1.894(1.744)	-0.15
CanESM2 (CanESM5)	1.633(1.498)	-0.135
ACCESS1-3 (ACCESS-CM2)	1.566(1.526)	-0.04
GISS-E2-R (GISS-E2-1-G)	1.717(1.687)	-0.03
CNRM-CM5 (CNRM-CM6-1)	1.492(1.472)	-0.02
bcc-csm1-1 (BCC-ESM1)	1.62(1.6)	-0.02
HadGEM2-ES (UKESM1-0-LL)	1.394(1.376)	-0.019
FGOALS-g2 (FGOALS-g3)	1.47(2.076)	0.606

annual mean and the seasonal reversion of the atmospheric cross-equatorial energy transport. To calculate the atmospheric cross-equatorial energy transport, we utilized the formulation of the atmospheric energy balance (Liu et al. 2022; Loeb et al. 2016; Trenberth et al. 2019).

Ignoring the small kinetic energy, the vertically integrated atmospheric energy balance can be written as follows (Peixoto and Oort 1992):

$$\nabla \cdot AET = F_{net} - \frac{\partial \langle E \rangle}{\partial t}, \quad (5)$$

where  $AET = \langle \vec{v}h \rangle$  is the atmospheric energy transport,  $\vec{v}$  is the horizontal wind,  $h = c_p T + gz + Lq$  denotes the moist static energy (MSE),  $\frac{\partial \langle E \rangle}{\partial t}$  is the energy storage term, where  $E = c_p T + Lq$  is the moist enthalpy of the atmosphere,  $\langle * \rangle$  indicates a mass-weighted vertical integral for the atmosphere column, i.e.,  $\frac{1}{g} \int_{P_t}^{P_s} * dp$ , where  $P_s$  is the pressure at the surface (varying with the coordinate of latitude and longitude) and  $P_t$  is pressure at the top of the troposphere (100 hPa), and  $F_{net}$  is the net energy input from the top of atmosphere (TOA) and surface.  $F_{net}$  could be further divided as follows:



$$F_{net} = SWA + LWC + STF, \tag{6}$$

where *SWA* is the total solar radiation absorbed by the atmosphere; *LWC* is the net longwave radiation cooling of the atmosphere, which is negative if longwave radiation is cooling the atmosphere; *STF* denotes the surface turbulent heating flux.

The observed surface turbulent heating flux (*STF*) is estimated using the residual method, which calculates the *STF* as difference between the net radiative input (from CERES EBAF; Kato et al. 2018; Loeb et al. 2018) and the total column atmospheric energy divergence and tendency (from mass-corrected ERA5; Mayer et al. 2021). In contrast to the observation, the simulated *STF* is directly obtained from the CMIP6 model output of surface energy budget, calculated as the sum of surface sensible and latent heating fluxes. Instead, the simulated  $\nabla \cdot AET$  is calculated as the residual of the net energy input  $F_{net}$  and the total energy tendency  $\frac{\partial(h)}{\partial t}$ , for the coarse temporal resolution to resolve transient eddies.

The southward cross-equatorial atmospheric energy transport can be expressed in terms of the inter-hemispheric contrast of atmospheric heating and the energy storage term (Donohoe et al. 2013). Based on the formula (5), a formulation similar to Donohoe et al. (2013) is used to decompose the cross-equatorial atmospheric energy transport into the inter-hemispheric contrast of the atmospheric heating:

$$AET_{EQ} = [SWA] + [STF] + [LWC] - \left[ \frac{\partial(E)}{\partial t} \right], \tag{7}$$

where  $[*]$  denotes the inter-hemispheric contrast, which is half the spatial integral of the Northern Hemisphere minus that in the Southern Hemisphere, as represented below:

$$[*] = \frac{1}{2}R^2 \left( \int_0^{\pi/2} \int_0^{2\pi} * \cos\theta d\lambda d\theta - \int_{-\pi/2}^0 \int_0^{2\pi} * \cos\theta d\lambda d\theta \right). \tag{8}$$

where  $\lambda$  denotes the longitude,  $\theta$  represents the latitude,  $AET_{EQ} = [\nabla \cdot AET]$  is the southward oriented cross-equatorial atmospheric energy transport, which is positive when the atmosphere transport energy from the Northern Hemisphere to the Southern Hemisphere.

### 2.5 Seasonal contrast and local seasonal contrast

The seasonal contrast  $\| * \|$  is defined as the difference between the mean of boreal summer half year (MJJASO: May, June, July, August, September, and October) and boreal winter half year (NDJFMA: November, December, January, February, March, and April). The formula of  $\| * \|$  is shown as follow:

$$\| * \| = \frac{\sum_{MJJASO} (*) - \sum_{NDJFMA} (*)}{6}. \tag{9}$$

Applying formula (8) onto formula (6), we get the inter-hemispheric energy budget of the seasonal contrast:

$$\|AET_{EQ}\| = \|[SWA]\| + \|[STF]\| + \|[LWC]\| - \left\| \left[ \frac{\partial(h)}{\partial t} \right] \right\|. \tag{10}$$

Correspondingly, the local seasonal contrast  $\| * \|_L$  is defined as the difference between local summer half year and local winter half year.

$$\|f(\lambda, \theta)\|_L = \begin{cases} \frac{\sum_{MJJASO} (f(\lambda, \theta)) - \sum_{NDJFMA} (f(\lambda, \theta))}{6}, & \theta \in (0^\circ, 90^\circ N] \\ \frac{\sum_{NDJFMA} (f(\lambda, \theta)) - \sum_{MJJASO} (f(\lambda, \theta))}{6}, & \theta \in [90^\circ S, 0^\circ) \end{cases} \tag{11}$$

where  $f$  is any horizontal physical field,  $\lambda$  denotes the longitude,  $\theta$  represent the latitude. The positive (negative)  $\|f(\lambda, \theta)\|_L$  means the  $f(\lambda, \theta)$  in the summer (winter) half year is more positive than that in the local winter (summer) half year. Note that the seasonal contrasts of the inter-hemispheric contrast are equal to the global integral of the local seasonal contrasts:

$$\int_{-\pi/2}^{\pi/2} \int_0^{2\pi} \|f(\lambda, \theta)\|_L \cos\theta d\lambda d\theta = \| [f(\lambda, \theta)] \|, \tag{12}$$

Based on above equation, we could attribute the terms in the inter-hemispheric energy budget of the seasonal contrast ( $\| * \|$ ) onto the local seasonal contrasts ( $\| * \|_L$ ) on the regional scale.

## 3 Results

### 3.1 Tropical precipitation bias in the CMIP5 and CMIP6

To evaluate the improvement from CMIP5 to CMIP6 models in the simulation of tropical precipitation, we first show the observation and multi-model ensemble mean (MEM) of scaled tropical precipitation of CMIP5 and CMIP6 models (Fig. 1). In the GPCP observation, ITCZ shows as a narrow rain belt over the Atlantic and eastern Pacific region, and is located at the north of the equator. Within the Indo-Pacific warm pool, the location of ITCZ shifts from 20°N in the boreal summer to 8°S in the boreal winter, which prompts an expansive precipitation distribution between 60°E to 180° (Fig. 1a). The observed pattern of tropical precipitation in the GPCP is consistent with that in the CMAP, with a pattern correlation of 0.96, ensuring the robustness of the observational precipitation (Fig. 1b).

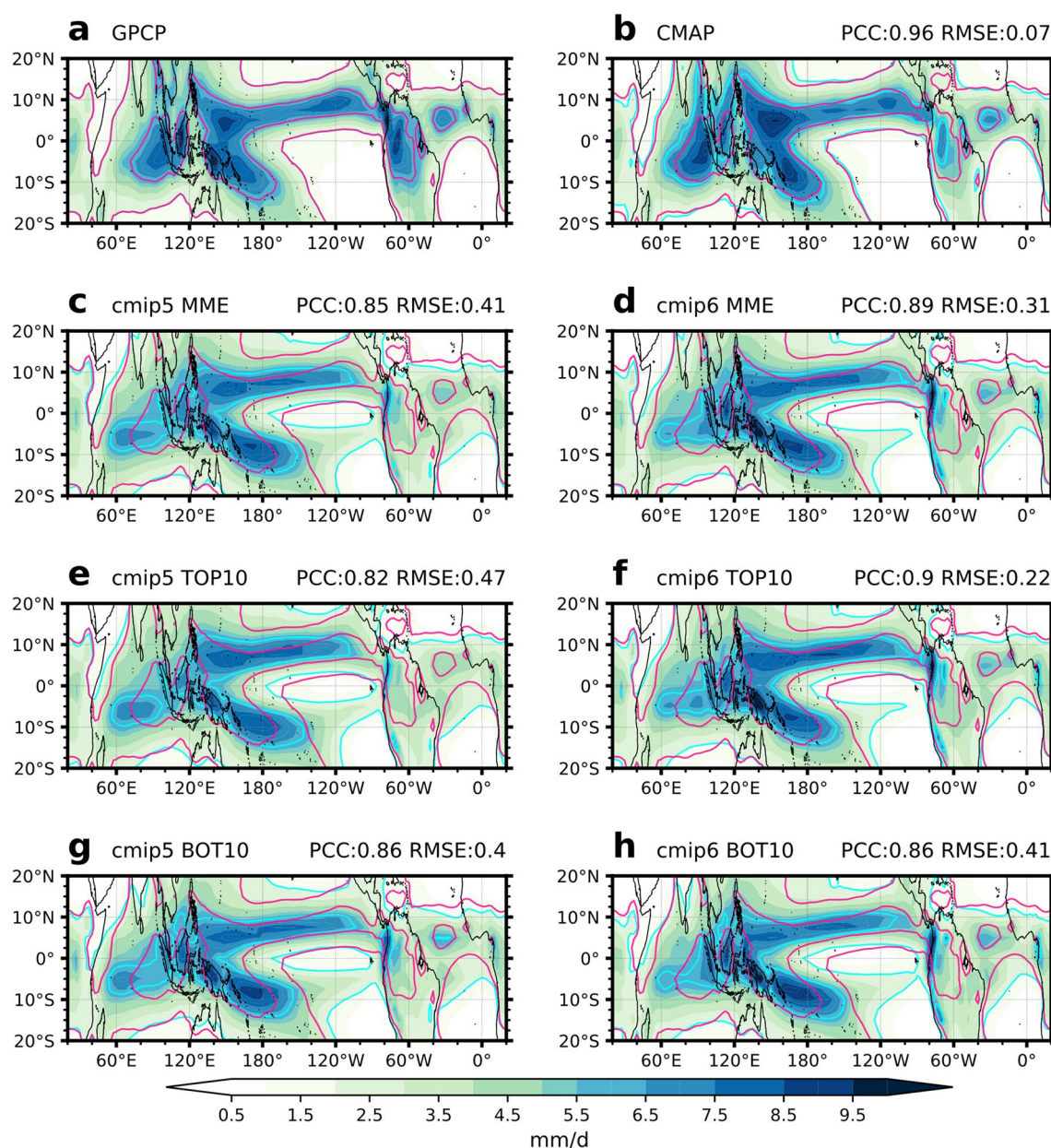


**Fig. 1** Scaled annual mean precipitation (unit:  $\text{mmday}^{-1}$ ) in the tropics ( $20^{\circ}\text{S}$  to  $20^{\circ}\text{N}$ ) from (a) GPCP observation, (b) CMAP observation, (c) CMIP5 MME, (d) CMIP6 MME, (e) CMIP5 TOP10 mean, (f) CMIP6 TOP10 mean, (g) CMIP5 BOT10 mean, (h) CMIP6 BOT10 mean. The deep pink (cyan) contour shows the  $2.6 \text{ mmday}^{-1}$  contour

Both the CMIP5 and CMIP6 models well reproduce the spatial distribution of observed tropical precipitation, with a pattern correlation coefficient (PCC) of 0.85 (0.89) relative to GPCP observation in the CMIP5 (CMIP6) MME. Compared to the CMIP5 MME, there is an improvement in the performance of tropical precipitation in the CMIP6 MME. The root-mean-square error (RMSE) decreases from  $0.41 \text{ mmday}^{-1}$  in CMIP5 to  $0.31 \text{ mmday}^{-1}$  in CMIP6 (Fig. 1c, d). On the regional scale, the North Pacific ITCZ

of GPCP (CMAP and simulations) precipitation. The pattern correlation coefficient (PCC) and root-mean-square error (RMSE; unit:  $\text{mmday}^{-1}$ ) of the spatial pattern relative to GPCP is labeled at the right top of (b-h)

displays insufficient strength over the eastern Pacific in the CMIP5 MME, while the South Pacific Convergence Zone (SPCZ) extends excessively towards the east (Fig. 1c). The equatorial Pacific cold tongue, indicated by the relatively small precipitation over the Pacific equator, appears to extend erroneously to the west in contrast to the observation. These features comprise the notorious Pacific "double ITCZ" bias in the CMIP5 models. Additionally, the ITCZ over the North Atlantic is weaker than

the observation, whereas the South Atlantic exhibits unrealistic large rainfall (Fig. 1c). The large-value center of the South Indian Ocean Convergence Zone (SIOCZ) erroneously lies in the central Indian Ocean, rather than west of Sumatra as in the observation. In the CMIP6 MMEM, the eastward extension of SPCZ and westward shift of SIOCZ are partly alleviated (Fig. 1d).

To identify the potential improvement that may be masked by the whole ensemble average, we further examined the tropical precipitation in the ensemble mean of TOP10 and BOT10 of CMIP5 and CMIP6. For the mean of CMIP5 TOP10, the tropical precipitation is similar with the MMEM with a PCC of 0.82 and a RMSE of  $0.47 \text{ mmday}^{-1}$  relative to GPCP observation (Fig. 1e). For the CMIP6 TOP10, the PCC increases to 0.9, and RMSE decreases to  $0.22 \text{ mmday}^{-1}$  (Fig. 1f). The main progress of the TOP10 models happened in the Pacific. The rainfall deficit in the western equatorial Pacific and North Eastern Pacific and the

surplus rainfall in the east of SPCZ are significantly reduced in CMIP6 (Fig. 1e, f). In contrast to the apparent improvement seen in the TOP10, the BOT10 in CMIP6 still shows systematic precipitation errors similar to those in CMIP5, with the PCC and RMSE remaining around 0.86 and  $0.4 \text{ mmday}^{-1}$ , respectively (Fig. 1g, h).

To further quantify the bias in the tropical precipitation distribution, we show the difference in the scaled precipitation between CMIP5 MMEM and GPCP observation. The CMIP5 models feature a typical “double ITCZ” bias in the MMEM with positive precipitation bias greater than  $3 \text{ mmday}^{-1}$  and  $2.5 \text{ mmday}^{-1}$  over the southern Pacific and Atlantic, respectively. Conversely, the models underestimate precipitation in the equatorial Western Pacific and North Eastern Pacific regions, west of Panama, by more than  $2 \text{ mmday}^{-1}$  (Fig. 2a). In the Indian Ocean, the MMEM bias in the precipitation shows a latitudinal dipolar pattern, with an underestimation of  $2 \text{ mmday}^{-1}$  west of Sumatra, and an

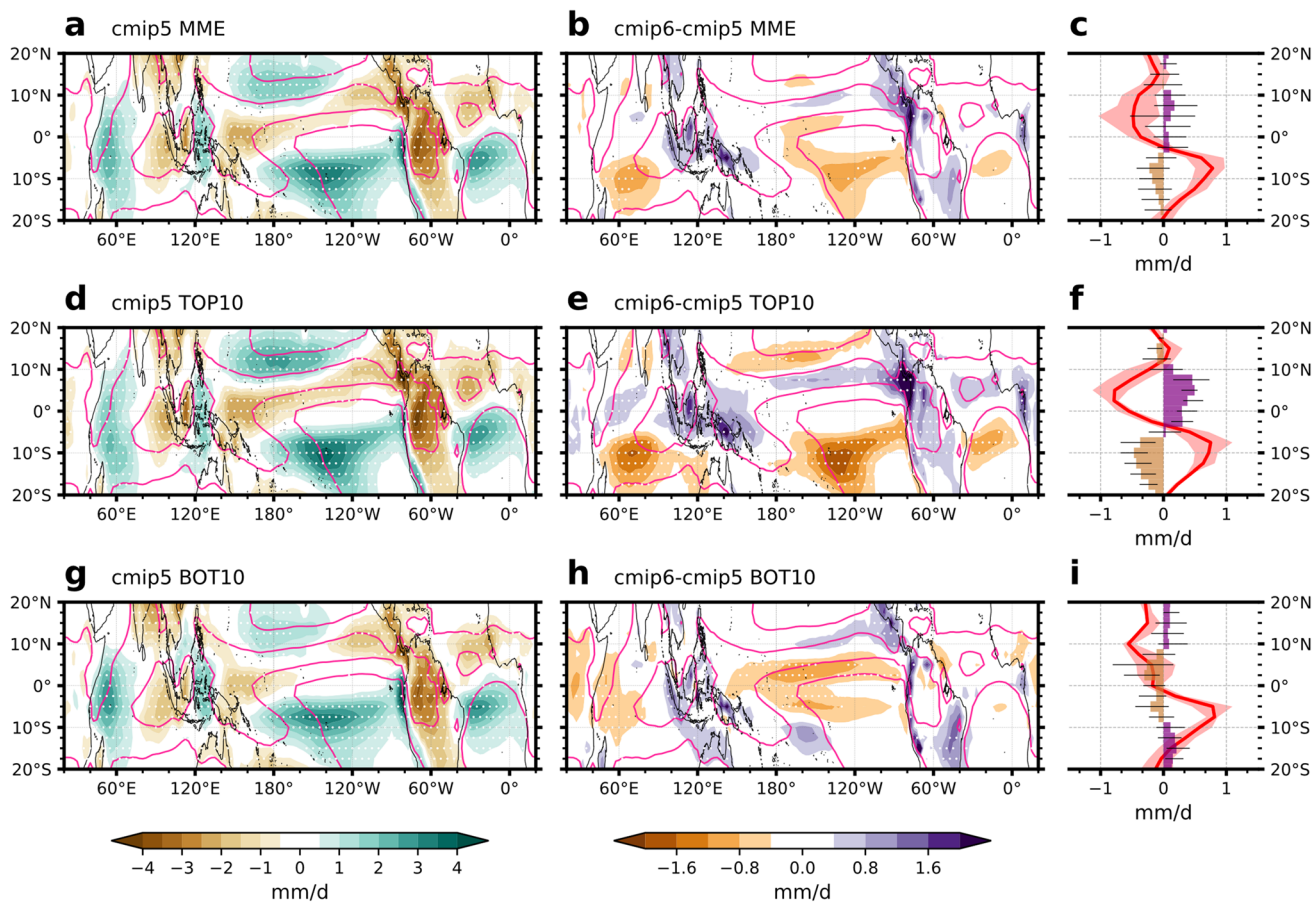


**Fig. 2** Scaled annual mean precipitation in the tropics for **a** the bias in CMIP5 MMEM relative to GPCP observation, **b** The change from CMIP6 MMEM to CMIP5 MMEM. **c** the bias in the zonal mean precipitation of CMIP5 MMEM (red profile) and the change from CMIP5 MMEM to CMIP6 MMEM (bars). Stippling denotes the area where at least 80% models agree on the sign of biases. shading and

error bars in (c, f, i) respectively denote the interquartile range of CMIP5 models and the change from CMIP5 to CMIP6. **d-f** and **(g-i)** are same as **(a-c)**, but for the mean of two sub-ensemble of CMIP5 (CMIP6) models, i.e. TOP10 and BOT10. The deep pink contour shows the  $2.6 \text{ mmday}^{-1}$  of GPCP precipitation



overestimation of  $2 \text{ mmday}^{-1}$  east of Africa (Fig. 2a). This Indian Ocean dipole bias mode has been traced back to errors in the South Asian summer monsoon (Li et al. 2015b).

The MMEM difference between CMIP6 and CMIP5 shows that, the positive biases in the southern Pacific and Atlantic are reduced by more than  $0.8 \text{ mmday}^{-1}$  (about 30% of the bias in CMIP5) and  $0.4 \text{ mmday}^{-1}$  (about 20% of the bias in CMIP5), respectively, within the major biased region (Fig. 2b). Additionally, the negative bias near the Panama is alleviated by more than  $1.2 \text{ mmday}^{-1}$  (about 60% of the bias in CMIP5) (Fig. 2b). Figure 2c exhibits the zonal mean precipitation bias of CMIP5 MMEM (red lines), and the change from CMIP5 to CMIP6 (bars). The meridional error pattern of the CMIP5 MMEM shows a typical hemispherical anti-symmetric mode that underestimates the inter-hemispheric contrast of tropical precipitation (Fig. 2c). Although the pattern of bias persists in the CMIP6, the magnitude of this latitudinal error is partly alleviated by about 20% in the CMIP6 (Fig. 2c). In summary, there is significant progress on MMEM precipitation between the two CMIP phases, however, for most regions the amount of progress is limited.

To reveal the potential improvement in certain models, we further investigated the precipitation bias in the TOP10 mean of CMIP5 and its change from CMIP5 to CMIP6. The error pattern of CMIP5 TOP10 shows similarity with the MMEM (Fig. 2d), with the most eminent bias occurring in the southern Pacific. In contrast to the limited improvement from CMIP5 to CMIP6 in the whole ensemble mean, the CMIP6 mean of TOP10 shows large alleviation over the Tropics in comparison with CMIP5, especially over the Pacific (Fig. 2e). The large-value center of positive bias over the Southeast Pacific of TOP10 mean in CMIP5 exceeds  $3.5 \text{ mmday}^{-1}$ . While, in CMIP6, it is reduced by more than  $1.6 \text{ mmday}^{-1}$ , which is nearly 50% of the bias in CMIP5 (Fig. 2d, e). The zonal mean precipitation bias of CMIP5 TOP10 shows deficit of precipitation over the northern Tropics and equator, and excessive rainfall over the southern Tropics (Fig. 2f). The magnitude of these biases is alleviated by about 50% in the CMIP6 (Fig. 2f). Different with the TOP10 models, the BOT10 bias in CMIP5 roughly persists in CMIP6 (Fig. 2g, h). Additionally, the width of BOT10 tropical precipitation seems to be further overestimated in CMIP6, with negative change over the deep-tropics of Pacific, and positive change in the poleward flanks of ITCZ and SPCZ (Fig. 2h, i).

In summary, from the perspective of pattern comparison, the CMIP6 models generally better catch the observed tropical precipitation than those in CMIP5. Significant improvement happened in the top ten models with larger reduction in the RMSE (TOP10). In contrast, the bottom ten models with smaller RMSE reduction (BOT10) show similar bias pattern in CMIP5 and CMIP6.

From the above results, it is clear that the tropical rainfall bias is characterized by a complex spatial distribution. To objectively depict the amplitude and spatial distribution of the zonal mean precipitation biases of the CMIP5 and CMIP6 models, the anti-symmetric and symmetric EOF analysis for zonal mean precipitation were used to extract the main bias features (Fig. 3). We first show the meridional distribution of the mean square of the zonal mean precipitation bias and its antisymmetric and symmetric components. The mean square of bias has bimodal peaks with a minimum of  $0.09 \text{ mm}^2/\text{day}^2$  at  $2.5^\circ\text{S}$  (Fig. 3a). The peak in the NH (SH) locates at the  $5^\circ\text{N}$  ( $7.5^\circ\text{S}$ ) with a value of  $0.54$  ( $0.6$ )  $\text{mm}^2/\text{day}^2$ . Poleward of these two peaks, the mean square decreases with increasing latitude. Furthermore, the bias could be divided into antisymmetric and symmetric components, with the total mean square being conservative (see Sect. 2.3). The antisymmetric component contributes 68.4% of the total mean square, with the peak of it locating at the  $7.5^\circ\text{N}$  and  $7.5^\circ\text{S}$  (blue bars in Fig. 3a). In contrast, the symmetric component contributes 31.6% of the total mean square, with its maximum at  $0^\circ$ , and two local peaks at  $10^\circ\text{N}$  and  $10^\circ\text{S}$  (magenta bars in Fig. 3a).

To clearly extract the antisymmetric and symmetric modes of the tropical precipitation biases, we respectively applied an EOF analysis to the antisymmetric and symmetric components of the scaled zonal-mean tropical precipitation biases (see Sect. 2.3). The first mode of antisymmetric (symmetric) component is denoted as ASYM (SYM), which explained 59.1% (19.5%) of the total mean square (Fig. 3b), and the corresponding PC is named ASYM-PC (SYM-PC) (Fig. 4). The ASYM represents the bias in the inter-hemispheric contrast of the tropical precipitation (Fig. 3b). Positive (negative) ASYM-PC indicates that the model overestimates (underestimates) the contribution of the Southern Hemisphere to the total tropical precipitation. The SYM characterizes the erroneous meridional expansion of the tropical precipitation (Fig. 3b). Positive (negative) SYM-PC indicates that the model overestimates (underestimates) the width of the meridional tropical precipitation distribution. To reveal the spatial patterns of tropical precipitation bias explained by the two leading modes, we regressed the inter-model spread of tropical precipitation distribution onto the ASYM-PC and SYM-PC. The regression pattern onto ASYM-PC shows a significant inter-hemispherical asymmetry of precipitation over the tropics, which is characterized by heavier rainfall in the Pacific ITCZ, north to the equator, and weaker rainfall in the Southeast Pacific where the traditional research on “double ITCZ” problem have focused on (Mechoso et al. 2016; Fushan et al. 2005; Lin 2007; Song and Zhang 2016; Si et al. 2021) (Fig. 3c). In contrast to ASYM-PC, the regression pattern onto SYM-PC shows heavier precipitation over the deep-tropics, and weaker precipitation over the poleward flanks of the main tropical rain

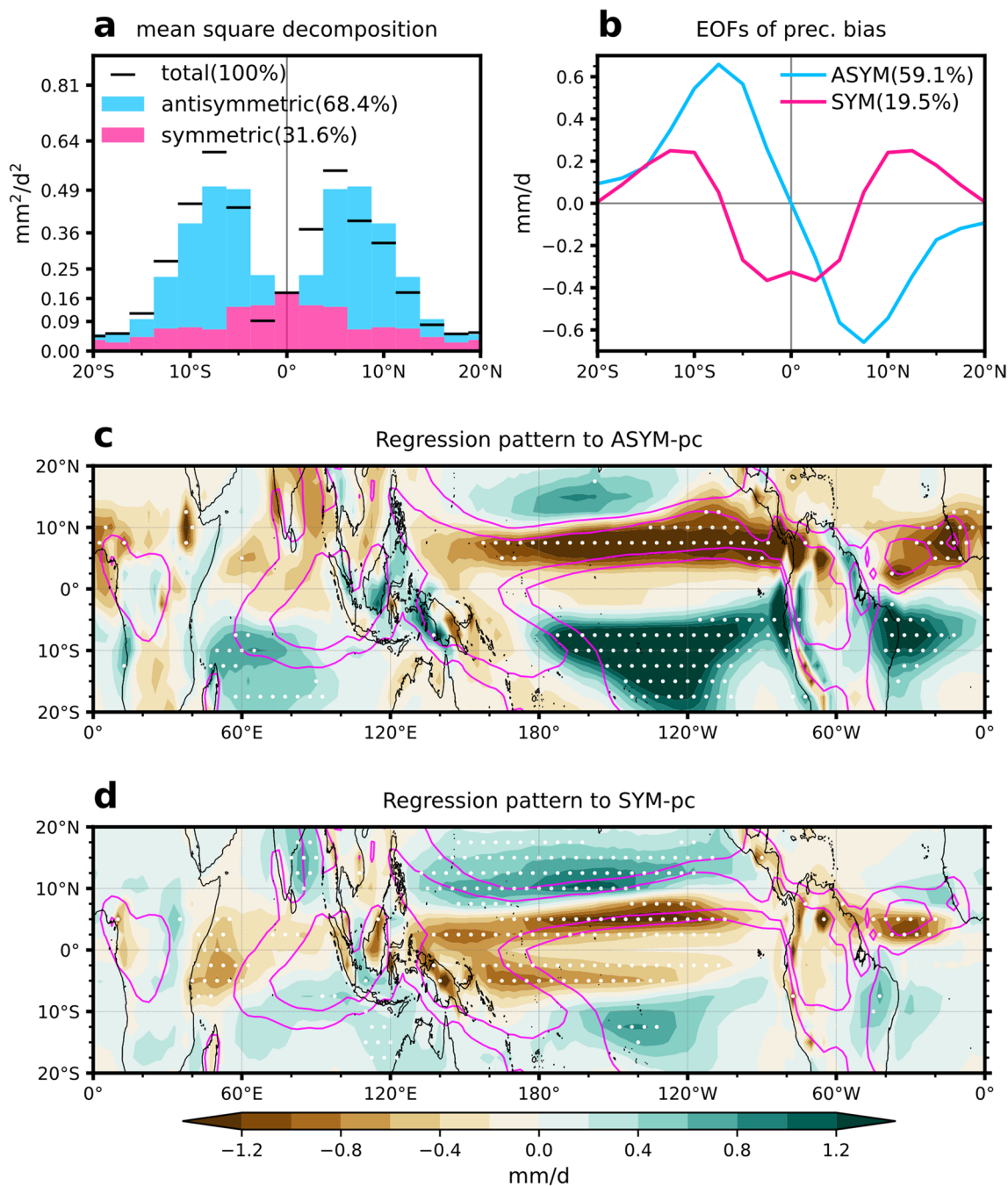


**Fig. 3** **a** The meridional distribution of the mean square of the biases in the zonal mean precipitation of CMIP5 and CMIP6 models (black short line), and its symmetric (magenta) and antisymmetric (blue) components. The percentages of their respective contributions to the total mean square are labeled in the upper left legend. **b** The first EOF modes of the antisymmetric (ASYM; blue) and symmetric (SYM;

magenta) components of the CMIP6 zonal mean precipitation bias. Their contribution to the total mean square are labeled in the legend. Regression patterns of scaled precipitation onto **(c)** ASYM-PC, **d** SYM-PC. The stippled regions in **(c, d)** represent where the regression is significant at the 99.9% confidence level

belts, such as North Pacific ITCZ, SACZ (South Atlantic Convergence Zone), SPCZ, and SIOCZ. The SYM indicates a shift of precipitation towards the equator (Fig. 3d).

Above analyses suggest that the bias in zonal mean tropical precipitation of CMIP6 models can be well represented

by the antisymmetric and symmetric bias modes with a total explained mean square of 78.6%. Further pattern regressions onto the ASYM-PC and SYM-PC show that the antisymmetric bias mode reflects precipitation contrast between the North Pacific ITCZ and the Southeast Pacific; and the



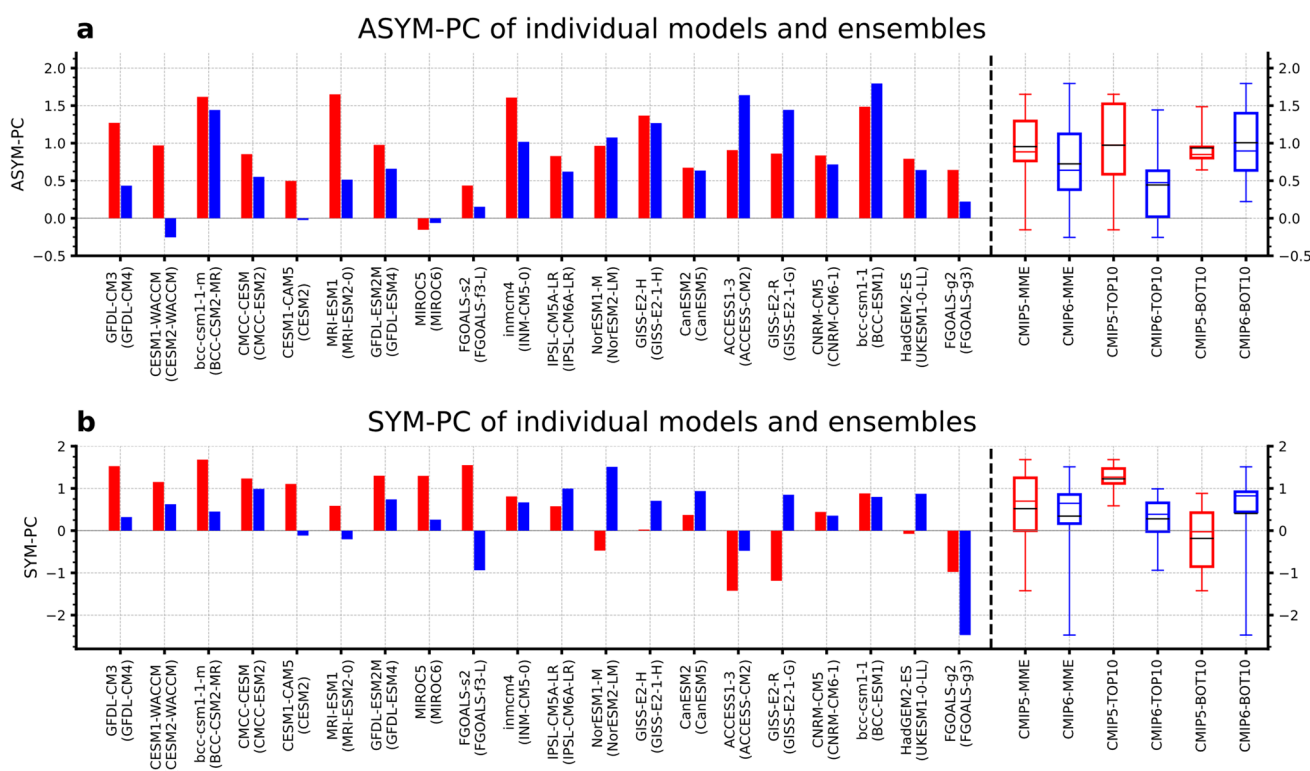


**Fig. 4** **a** the ASYM-PC of model pairs with prior versions in CMIP5 (red) and new versions in CMIP6 (blue, model name in the brackets). Bars show the PCs of individual model. Models are ordered according to the RMSE changes from CMIP5 to CMIP6 (from negative to positive). The boxes show the median and 25th to 75th percentiles of model ensemble, black short line in the boxes denotes the ensemble

symmetric mode reflects the width of precipitation in the tropical Pacific, which is linked to the seasonal migration of ITCZ.

To quantify the changes in the zonal mean tropical precipitation bias, we show the ASYM-PC and SYM-PC of individual CMIP5 models and their new versions in CMIP6. The absolute values of ASYM-PC and SYM-PC of the TOP10 models in CMIP6 are all smaller than those in CMIP5 (bars in Fig. 4). In contrast, from CMIP5 to CMIP6, 6 (4) of the 10 BOT10 models show a decrease in the absolute value of ASYM-PCs (SYM-PCs) (bars in Fig. 4).

The MMEM ASYM-PC of the CMIP5 (CMIP6) is 0.95 (0.72), with an interquartile range from 0.76 to 1.3 (0.38 to 1.1) (boxplots in Fig. 4a). The MMEM ASYM-PC in CMIP5 is reduced by 24% in CMIP6. The TOP10 mean ASYM-PC in CMIP5 is 0.97 (interquartile range from 0.59 to 1.52), while in CMIP6 it is 0.44 (interquartile range from 0.02 to 0.63). The TOP10 mean ASYM-PC is reduced by 54% in CMIP6 compared to CMIP5. As opposed to TOP10, the BOT10 ASYM-PC in CMIP6 is 1.0 (with an interquartile range of 0.64 to 1.4), which is 0.06 higher than that in CMIP5 (with an interquartile range of 0.8 to 0.95). Above

mean, whiskers denote the minimum and maximum. The boxplots of MME (ensemble of all 20 models), TOP10 (the ten most improved models from CMIP5 to CMIP6), and BOT10 (the ten least improved models from CMIP5 to CMIP6) of CMIP5 (red boxplots) and CMIP6 (blue boxplots) are shown in the right part. **b** as (a), but for the SYM-PC

results indicate that the antisymmetric bias in tropical precipitation has been reduced from CMIP5 to CMIP6, and this reduction is primarily due to the alleviation in the TOP10, i.e. the ten models with largest alleviation in the RMSE.

The MMEM SYM-PC is 0.52 in CMIP5 (with an interquartile range of 0.0 to 1.3) and decreased to 0.34 in CMIP6 (with an interquartile range of 0.17 to 0.86) (boxplots in Fig. 4b). Although the MMEM is reduced from CMIP5 to CMIP6, both MMEMs of CMIP5 and CMIP6 fall within the interquartile range of each other. Additionally, the alleviation in the MME median of SYM-PC is weak, only decreasing from 0.70 in CMIP5 to 0.65 in CMIP6. Thus, the improvement of MMEM SYM-PC is contributed by individual models, rather than a general improvement in the majority of models. Different with MME, the SYM-PC of TOP10 (BOT10) shows significant alleviation (exacerbation). The TOP10 (BOT10) mean SYM-PC in CMIP5 is 1.22 (-0.18), and in CMIP6 it is 0.28 (0.41), with an interquartile range of 1.12 to 1.47 (-0.85 to 0.43) and -0.02 to 0.66 (0.44 to 0.92), respectively. The TOP10 mean SYM-PC is reduced by 77% in CMIP6 compared to CMIP5, and the absolute value of BOT10 mean SYM-PC is enlarged by 122%.

In summary, The ASYM-PC, which reflects the bias in the hemispheric contrast of tropical precipitation, is generally alleviated from CMIP5 to CMIP6. This improvement is predominantly due to the changes in the TOP10 models. The TOP10 mean of ASYM-PC is reduced by 54% from CMIP5 to CMIP6. Furthermore, the SYM-PC, indicating the bias in the width of tropical precipitation, shows no significant improvement in the whole model ensemble between two phases of CMIP. While the TOP10 mean SYM-PC is largely reduced by 77% from CMIP5 to CMIP6.

### 3.2 Atmospheric energetics underlying the bias in hemispheric contrast of tropical precipitation

The hemispheric contrast of tropical precipitation is constrained by the cross-equatorial atmospheric energy transport ( $AET_{EQ}$ ). To explore the possible mechanism behind the antisymmetric biases of tropical precipitation, we analyzed

the correlation between ASYM-PC and the biases in the annual mean cross-equatorial atmospheric energy transport for both CMIP5 and CMIP6 models. The result shows that the inter-model spread of ASYM-PC is significantly correlated with the annual mean  $AET_{EQ}$  with  $R = -0.7$  when excluding two outlier model pairs (Fig. 5a). We also examined the relationship between the changes of ASYM-PC and  $AET_{EQ}$  from CMIP5 to CMIP6. Their changes show a significant inter-model correlation with  $R = -0.88$ , indicating that the alleviation in the tropical precipitation hemispheric contrast may stem from the more realistic atmospheric energetics in a subset of the CMIP6 models (Fig. 5b).

There are six model pairs of the TOP10 with negative CMIP5-to-CMIP6 changes in the ASYM-PC and positive changes in the  $AET_{EQ}$ . They are GFDL-CM3 (GFDL-CM4), CESM1-WACCM (CESM2-WACCM), bcc-csm1-1-m (BCC-CSM2-MR), CMCC-CESM (CMCC-ESM2), CESM1-CAM5 (CESM2), MRI-ESM1 (MRI-ESM2-0), GFDL-ESM2M (GFDL-ESM4), and inmcm4 (INM-CM5-0) (triangles in

**Fig. 5** **a** Scatter plot between ASYM-PC and annual mean southward cross-equatorial atmospheric energy transport ( $AET_{EQ}$ ) bias of the CMIP5 (red) and CMIP6 (blue) models. **b** Scatterplot between changes in the ASYM-PC and  $AET_{EQ}$  from CMIP5 version to CMIP6 version for each model pairs. The highlight (triangle) denotes the six TOP10 models with negative changes in the ASYM-PC and positive changes in the  $AET_{EQ}$  from CMIP5 to CMIP6, the big triangles show the mean of them. The black solid line marks the least squares linear fit across all model experiments with correlation coefficient labeled at the right top. The asterisk indicates regression significant at the 99% confidence level, while the double asterisk indicates regression significant at the 99.9% confidence level. Linear regression and correlation coefficients in (a, b) are calculated when excluding CESM1-WACCM (CESM2-WACCM) and FGOALS-s2 (FGOALS-f3-L) models (plus signs)

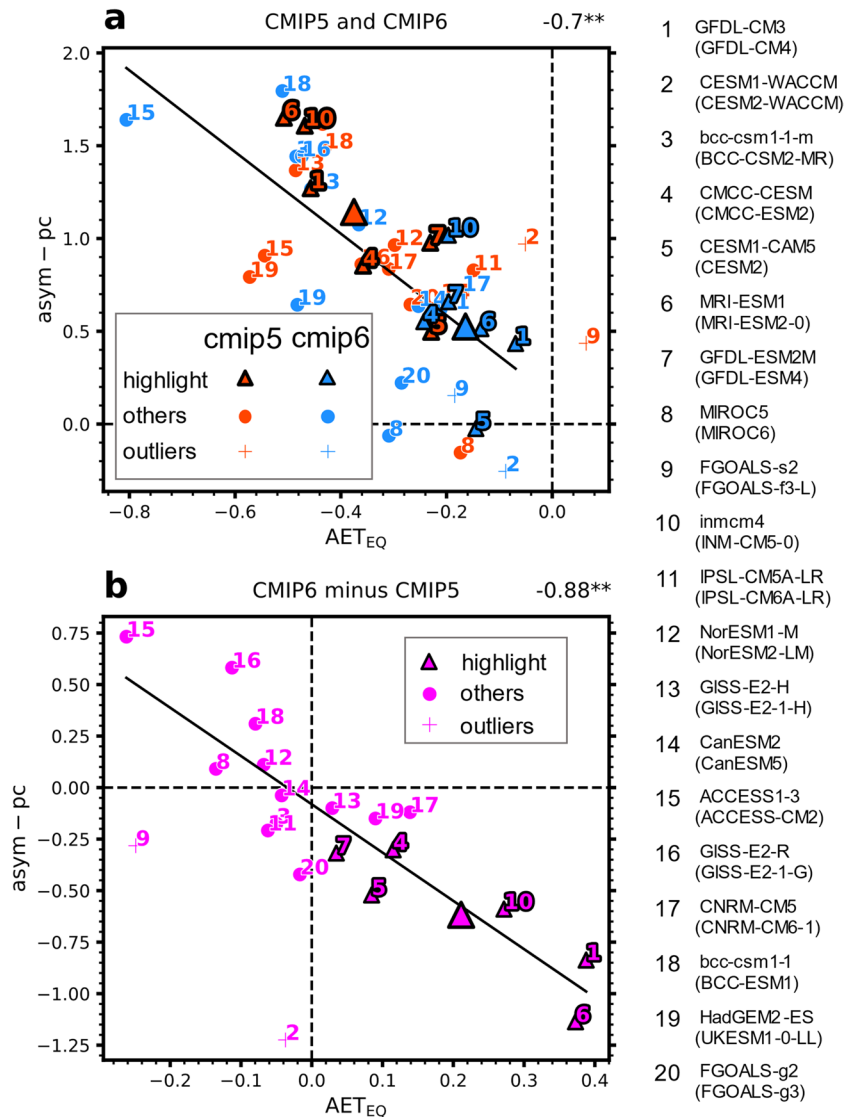


Fig. 5). The mean ASYM-PC of the six models is 1.14 in CMIP5 and decreases to 0.53 in CMIP6, which is reduced by 54% (Fig. 5). The ASYM-PC changes of the six highlighted model pairs account for the bulk changes of TOP10. Correspondingly, the  $AET_{EQ}$  bias of the mean of the six models is -0.38 PW in CMIP5 and decreased to -0.16 PW in CMIP6, which is reduced by 58% (Fig. 5). The alleviation of ASYM-PC in TOP10 models is associated with the reduction of  $AET_{EQ}$  bias.

To further understand the contribution of different atmospheric heating terms to the reduction of the  $AET_{EQ}$  bias from CMIP5 to CMIP6 in the TOP10, we diagnosed the closed interhemispheric energy budgets (see Sect. 2.4) of the observation, and the aforementioned six TOP10 model pairs selected by the sign of CMIP5-to-CMIP6 changes of ASYM-PC (negative) and  $AET_{EQ}$  (positive). The observed southward cross-equatorial atmospheric energy transport  $AET_{EQ}$  is 0.33PW (hollow green bars in Fig. 6a). The observed hemispheric contrast of  $SWA$  (total solar radiation absorbed by the atmosphere) and  $LWC$  (net atmospheric cooling by longwave radiation) are, respectively, 0.49 PW and 0.37 PW, implying that the solar (longwave) radiation in the Northern Hemisphere (Southern Hemisphere) heats (cools) the atmosphere by 0.98 PW (0.74 PW) more than that in the Southern Hemisphere (Northern Hemisphere) (Fig. 6a). Against to the  $[SWA]$  and  $[LWC]$ , the hemispheric contrast of  $STF$  (surface turbulent heat flux) is -0.53 PW, which means the surface turbulent heat flux in the Southern Hemisphere heats the atmosphere by 1.06 PW more than that in the Northern Hemisphere (Fig. 6a). The hemispheric contrasts in the  $SWA$ ,  $LWC$ , and  $STF$  are largely compensated, and their net budget determines the cross-equatorial atmospheric energy transport in the observation.

For the mean of the six highlighted TOP10 models, the cross-equatorial energy transport is -0.05 PW in CMIP5, which is underestimated by 0.38 PW compared to the observation, and this underestimation is mainly contributed by the  $[STF]$  (-0.23 PW), and the  $[SWA]$  (-0.11 PW) (Fig. 6a and b). In CMIP6, there is an increase of 0.21 PW in  $AET_{EQ}$  compared to CMIP5. The mean  $AET_{EQ}$  in CMIP6 approaches 42% of observed value. It is worth noting that 55% of the increase in  $AET_{EQ}$  could be attributed to the alleviation of the negative  $[STF]$  bias, which is decreased by 0.12 PW.

In summary, above analyses suggest that the improvement of the annual mean  $AET_{EQ}$  in the TOP10 models from CMIP5 to CMIP6 mainly stems from the decreased negative bias in  $[STF]$ .

To identify the regional sources contributing to the reduction of the  $[STF]$  bias in the aforementioned six TOP10 model pairs from CMIP5 to CMIP6, we compared the STF pattern simulated by them with the observation and analyzed the differences between the two CMIP phases. In the observation, the zonal integrals of STF

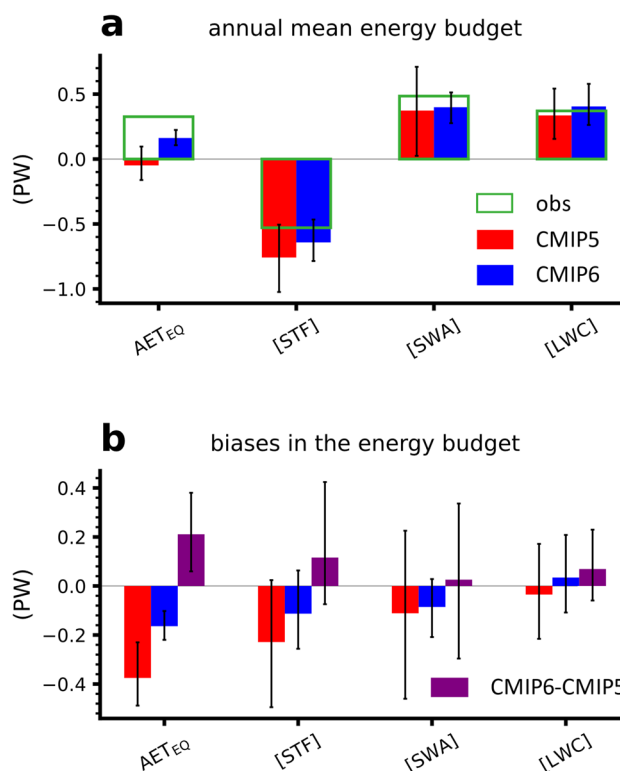


**Fig. 6** **a** Annual mean interhemispheric energy budget for the observation (hollow green bars) and the six highlighted models in TOP10 in CMIP5 (red bars) and CMIP6 (blue bars). The six highlighted model pairs all feature negative CMIP5-to-CMIP6 changes in the ASYM-PC and positive changes in the  $AET_{EQ}$ . According to the formulation of the interhemispheric energy budget, the annual mean cross-equatorial energy transport ( $AET_{EQ}$ ) is determined by the hemispheric contrasts (see Method for the definition) in three kinds of the atmospheric heating: surface turbulent heat flux ( $[STF]$ ), total solar radiation absorbed by the atmosphere ( $[SWA]$ ), net atmospheric cooling by longwave radiation ( $[LWC]$ ). The positive value in this budget means the corresponding heating process heats (cools) the atmosphere in the Northern hemisphere more (less) than in the Southern Hemisphere. The error bars show the 10th to 90th percentiles of model ensembles. **b** as (**a**), but for the model bias with respect to observation. The differences between CMIP6 and CMIP5 are shown by the purple bars

feature a minimum near the equator, peak at the 10°N and 15°S, and decreases with the growing latitudes at higher latitudes (lines in Fig. 7a). Tropical (extratropical) STF in the Southern Hemisphere is higher (lower) than in the Northern Hemisphere (bars in Fig. 7a; b). In the Tropics (5° ~ 30°), the higher STF in the Southern Hemisphere compared to the Northern Hemisphere is largely due to the contrast between the Afro-Asia regions and the South Indian Ocean Convergence Zone, as shown in Fig. 6b. In the extra-tropical region (30° ~ 70°), the hemispheric difference in the STF is dominated by the northward cross-equatorial heat transport of the oceanic meridional overturning circulation (MOC) (Frierson et al. 2013). This



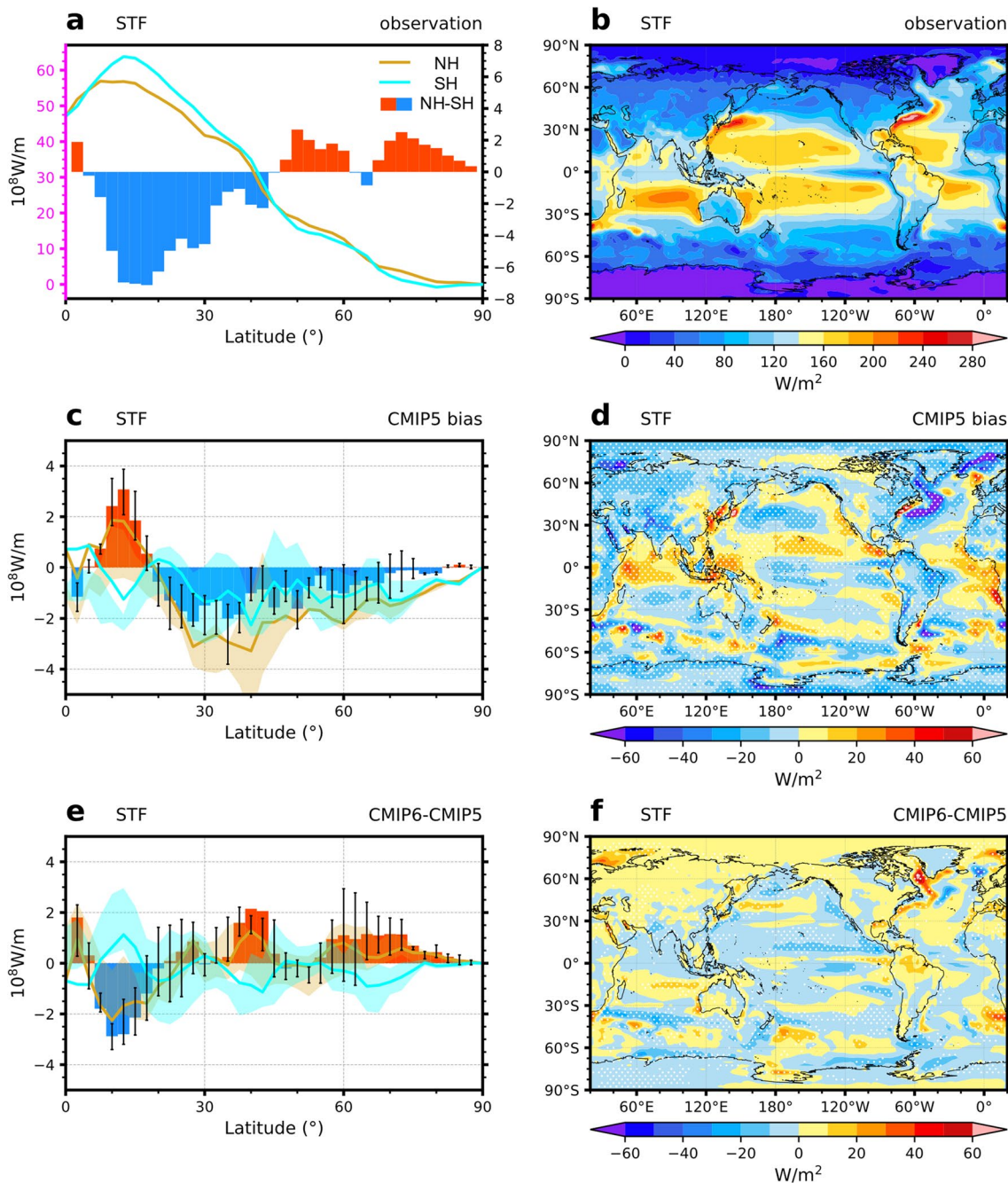


**Fig. 7** **a** distance-weighted zonal integral of the observed surface turbulent flux (*STF*) inferred by the residual of ERA5 reanalysis and CERES radiation product. The brown (sky blue) lines denote the Northern Hemisphere NH (Southern Hemisphere SH), bars correspond to NH minus SH difference. **b** spatial pattern of observed *STF*. **c**, **d** same as (**a**, **b**), but for the mean bias of the six selected TOP10 models, which all feature negative CMIP5-to-CMIP6 changes

in the ASYM-PC and positive changes in the  $AET_{EQ}$  in CMIP5. The interquartile range of the six CMIP5 models are denoted by shading (brown for SH, cyan for NH) and error bars (SH minus NH difference) in (**c**). The stippling in (**d**) denotes the area where at least five in the six models agree on the sign of biases. **e**, **f** same as (**a**, **b**), but for the difference between the CMIP6 and CMIP5

MOC linked deep water production in the North Atlantic with the upwelling in the Southern Ocean, and thus facilitated the hemispheric difference of extra-tropical STF (Fig. 7b).

Compared to observation, the mean of the selected CMIP5 models underestimates the zonal integral of STF at nearly all the subtropical and extra-tropical latitudes ( $> 20^\circ$ ) (lines in Fig. 7c), and overestimates (underestimates) it in

lower latitudes ( $5^{\circ} \sim 20^{\circ}$ ) of NH (SH). The underestimation in the subtropical and extra-tropical region is stronger in NH than that in SH, dominating the negative [STF] bias (bars in Fig. 7c). Regionally, there is an extensive and consistent negative bias in the Northern Hemisphere, especially in the regions of Afro-Asia, North Pacific, Gulf Stream, Labrador Sea, and Nordic Seas (Fig. 7d). On the other hand, the negative bias in the Southern Hemisphere exhibits a larger zonal contrast. This hemispherically distinct bias pattern results in the negative [STF] bias.

Figure 7e, f show the STF pattern change of the aforementioned six models between the two CMIP phases. Compared to CMIP5, the dipole bias in the lower-latitude tropics ( $0^{\circ} \sim 20^{\circ}$ ) gets significant alleviation in CMIP6. This improvement may be due to the local feedback of SST and surface wind resulting from the ITCZ shift. In the extra-tropical region ( $30^{\circ} \sim 70^{\circ}$ ), the negative bias of zonal integral of STF in the NH (SH) is alleviated (enhanced) in CMIP6, and thus dominates the significant decrease in the negative [STF] bias (Fig. 7e). On the regional scale, the biases in the Labrador Sea, Gulf Stream regions, and Nordic Seas in the NH are largely alleviated in CMIP6 (Fig. 7f). These improvements reduce the negative STF bias in the Northern Hemisphere. In contrast, negative change in STF from CMIP5 to CMIP6 is observed in the regions over the South Indian and South Pacific currents, as well as most seas around Antarctica. These changes lead to the enlargement of negative bias in Southern Hemisphere.

In summary, the reduction of the [STF] bias in the six selected model pairs from CMIP5 to CMIP6 is mainly due to a reduction (increase) of the negative STF bias in the extratropical region of the NH (SH). Regionally, the changes over the North Atlantic Ocean and Southern Ocean significantly contribute to the decrease of [STF].

### 3.3 Atmospheric energetics underlying the bias in width of tropical precipitation

As opposed to the antisymmetric mode (ASYM), the symmetric mode (SYM) represents the width of annual mean tropical precipitation. The width of the tropical precipitation corresponds to the range of the seasonal shift of ITCZ (Donohoe et al. 2019; Kim et al. 2021). To explore the possible mechanism underlying the symmetric biases of tropical precipitation, we examined the correlation coefficient between SYM-PC and the bias in the seasonal contrast of cross-equatorial atmospheric energy transport ( $\|AET_{EQ}\|$ ) for both CMIP5 and CMIP6 models (see Sect. 2.5 for the definition of seasonal contrast). The inter-model spread of SYM-PC is significantly correlated with the  $\|AET_{EQ}\|$ , with  $R = 0.62$  (Fig. 8a). Given the energetics constraint of seasonal shift of ITCZ (Donohoe et al. 2019), a smaller  $\|AET_{EQ}\|$  implies a weaker seasonal shift of ITCZ, which

corresponds to a narrower meridional distribution of annual mean precipitation in the tropics, and thus a larger SYM-PC. Note that the linear regression line in the Fig. 8b does not pass through the origin of coordinate, which indicates that the symmetric mode will be biased even with perfect  $\|AET_{EQ}\|$ . Furthermore, their changes from CMIP5 to CMIP6 show a significant inter-model correlation with  $R = 0.86$ . This result suggests that the increased accuracy in the simulated width of the tropical precipitation is likely a result of changes in the atmospheric energetics in a subset of the CMIP6 models (Fig. 8b).

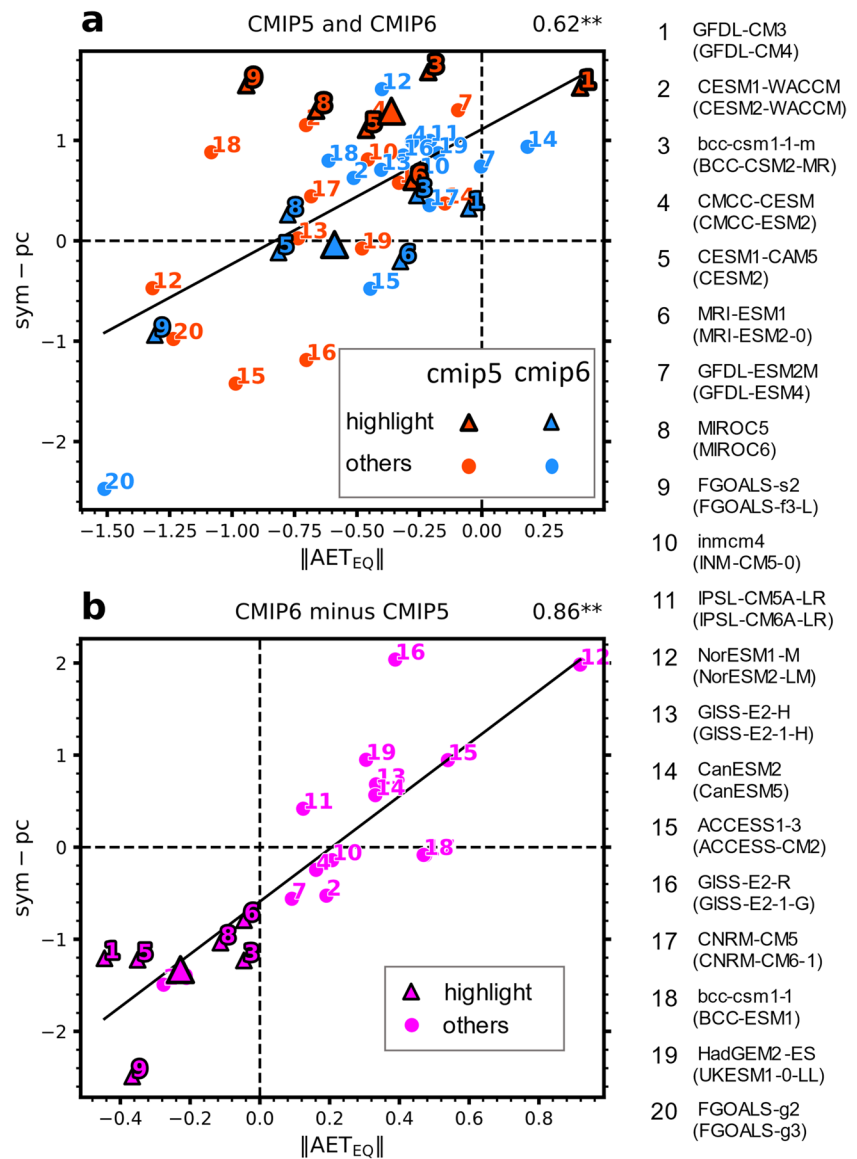
There are six model pairs in the TOP10 with negative CMIP5-to-CMIP6 changes in the SYM-PC and negative changes in the  $\|AET_{EQ}\|$ . They are GFDL-CM3 (GFDL-CM4), bcc-csm1-1-m (BCC-CSM2-MR), CESM1-CAM5 (CESM2), MRI-ESM1 (MRI-ESM2-0), MIROC5 (MIROC6), and FGOALS-s2 (FGOALS-f3-L) (triangles in Fig. 8). The averaged SYM-PC of the above six model pairs is 1.29 in CMIP5 and decreases to -0.04 in CMIP6, which is decreased by nearly 103% (Fig. 8). Correspondingly, the mean of  $\|AET_{EQ}\|$  of the six model pairs is negatively biased by 0.36 PW in CMIP5, while the negative bias increases to 0.59 PW in CMIP6, which is increased by 63% from CMIP5 to CMIP6. The alleviation of SYM-PC of certain models in CMIP6 is associated with the enlargement of the negative  $\|AET_{EQ}\|$  bias.

To further understand the contribution of different atmospheric heating terms to the seasonal contrast of the cross-equatorial energy transport ( $\|AET_{EQ}\|$ ), we examined the closed Hemispheric energy budget for the seasonal contrast in both the observation and the aforementioned six TOP10 models, which is selected by negative changes in  $\|AET_{EQ}\|$  and SYM-PC from CMIP5 to CMIP6. Similar with the annual mean  $AET_{EQ}$ , the seasonal contrast of  $AET_{EQ}$  is largely balanced by the seasonal contrasts of the hemispheric contrast in  $STF$ ,  $SWA$ , and  $LWC$ . However, in the monthly time scale, the seasonal change of the atmospheric energy storage should not be ignored. Therefore, in the budget of seasonal contrast we kept the atmospheric storing term  $\left\| \left[ \frac{\partial(E)}{\partial t} \right] \right\|$ . In the observation, the seasonal contrast of  $AET_{EQ}$  (3.53 PW) is mainly driven by the seasonal contrast of  $[SWA]$  (7.7 PW), with all the other heating process compensating the solar radiation (hollow green bars in Fig. 9a). The seasonal contrast of  $[STF]$ ,  $[LWC]$ , and  $-\left[ \frac{\partial(E)}{\partial t} \right]$  are respectively -2.36 PW, -1.85 PW, and 0.05 PW (Fig. 9a).

Both the CMIP5 and CMIP6 versions of the six TOP10 models selected by  $\|AET_{EQ}\|$  and SYM-PC well capture the bulk of the observed seasonal contrast of hemispheric contrast of energy budget (Fig. 9a). The mean  $\|AET_{EQ}\|$  of the six selected models in CMIP5 (CMIP6) is 3.16 (2.94) PW, which is 0.36 (0.59) PW lower than the observation. The enlargement of negative  $\|AET_{EQ}\|$  bias from CMIP5 to



**Fig. 8 a** Scatter plot between SYM-PC and the seasonal contrast of cross-equatorial atmospheric energy transport ( $\|AET_{EQ}\|$ ) bias of the CMIP5 and CMIP6 model pairs.  $\| * \|$  denotes the seasonal contrast which is defined as the difference between summer half year (May, June, July, August, September, and October) and winter half year (November, December, January, February, March, and April). **b** Scatterplot between changes in the SYM-PC and  $\|AET_{EQ}\|$  from CMIP5 version to CMIP6 version of each model pairs. The highlight (triangle) denotes the six model pairs in the TOP10 with negative SYM-PC and  $\|AET_{EQ}\|$  changes, the big triangles show the mean of them. The black solid line marks the least squares linear fit across all model experiments with correlation coefficient labeled at the right top. The asterisk indicates regression significant at the 99% confidence level, while the double asterisk indicates regression significant at the 99.9% confidence level



CMIP6, is dominated by the reduction of positive  $\| [STF] \|$  bias. The mean  $\| [STF] \|$  is -2.0 PW in CMIP5 and overestimated by 0.36 PW compared to the observation. In contrast, the mean  $\| [STF] \|$  decreases to -2.5 PW in CMIP6, which is 0.51 PW more negative than in CMIP5 (Fig. 9). 55% of the CMIP5-to-CMIP6 change in  $\| [STF] \|$  is compensated by the changes in  $\| [SWA] \|$ ,  $\| [LWC] \|$ , and  $\| \left[ \frac{\partial(E)}{\partial t} \right] \|$ , and the remaining 45% is balanced by the change in  $\| AET_{EQ} \|$  (Fig. 9b).

In summary, the CMIP5-to-CMIP6 enlargement of bias in the seasonal contrast of the cross-equatorial energy transport ( $\| AET_{EQ} \|$ ) of the selected six TOP10 models is dominated by the  $\| [STF] \|$ .

The seasonal contrasts of the hemispheric contrast of any global 2-dimension physical fields (such as  $STF$ ,  $SWA$ ), are equal to the global integral of the local

seasonal contrasts ( $\| * \|_L$ ) of these global physical fields (see Sect. 2.5). To identify the regional contribution to the reduction of  $\| [STF] \|$  bias of the aforementioned six TOP10 models selected by negative changes in  $\| AET_{EQ} \|$  and SYM-PC from CMIP5 to CMIP6, we compared simulated local seasonal contrast of  $STF$  ( $\| STF \|_L$ ) with the observation and displayed the differences between the two CMIP phases. In the observation, the  $STF$  over the land (ocean) area generally peaks in the local summer (winter), therefore the land (ocean) area typically has positive (negative)  $\| STF \|_L$  (Fig. 10a). In the Northern Hemisphere, the Kuroshio and Gulf regions serve as centers of large negative  $\| STF \|_L$  (Fig. 10a). The zonal integral of the LSC of  $STF$  is negative at most latitudes, except the latitudes with relatively broad landmass, such as Antarctica, Asia, and North America (Fig. 10b).

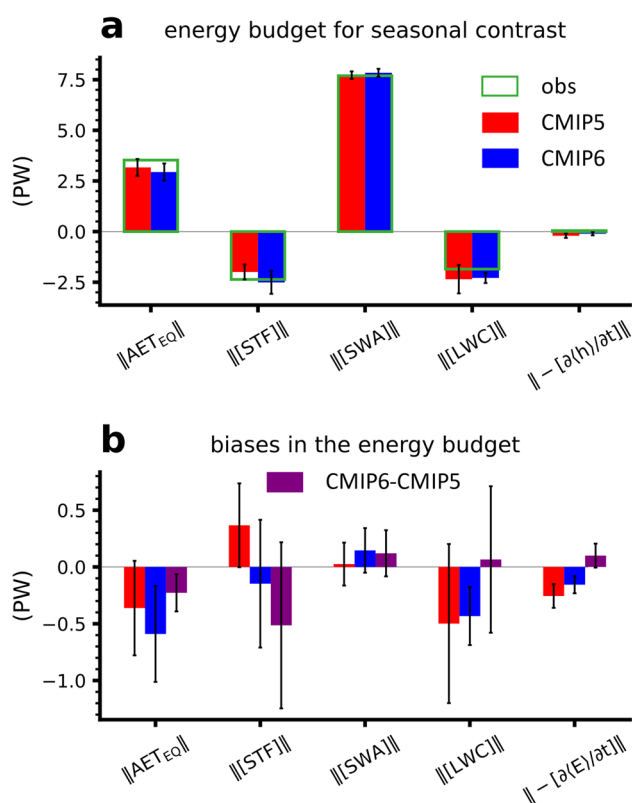


**Fig. 9** **a** interhemispheric energy budget of the seasonal contrast for the observation (hollow green bars), CMIP5 (red bars) and CMIP6 (blue bars) mean of the selected six TOP10 model pairs. The selected six TOP10 model pairs all feature negative CMIP5-to-CMIP6 changes in the SYM-PC and the  $\|AET_{EQ}\|$ . The error bars show the 10th to 90th percentiles of model ensembles. According to the formulation of the interhemispheric energy budget, the seasonal contrast of cross-equatorial energy transport ( $\|AET_{EQ}\|$ ) is determined by the hemispheric contrasts (see Sect. 2.5 for the definition of seasonal contrast) in four kinds of the atmospheric heating, as elaborated in the Fig. 6, and the atmospheric energy storing  $\left[\frac{\partial(E)}{\partial t}\right]$ .  $\| * \|$  denotes the seasonal contrast which is defined as the difference between extended boreal summer (May, June, July, August, and September) and extended boreal winter (November, December, January, February, and March). **b** as (**a**), but for the bias with respect to observation. Additionally, the results of CMIP6 minus CMIP5 are denoted by the purple bars in (**b**)

The  $\|STF\|_L$  bias of the selected six models in CMIP5 exhibits zonally consistent negative bias in the deep-tropical ocean (Fig. 10c). In contrast, the positive bias dominates subtropics and extratropical regions in both hemispheres. In the NH, the Barents Sea, Greenland Sea, Labrador Sea, and Gulf Stream regions feature positive bias larger than  $30 W/m^2$ , and the high-latitude parts of North Pacific Ocean and the bulk of Arctic Ocean also show consistent positive bias (Fig. 10c). In contrast, the sea area to the south of Iceland exhibits a substantial negative bias ( $18 \sim 30 W/m^2$ ), and consists of a zonal dipole pattern with the positive bias in the western region of the North Atlantic Ocean. In the

SH, more than 80% area in the subtropical and extra-tropical region ( $20^\circ S$  to  $90^\circ S$ ) shows a systematic positive error, and the Southern Ocean exhibits the greatest positive bias among the Southern Hemisphere (Fig. 10c). For the zonal integral of  $\|STF\|_L$ , The CMIP5 bias shows significant positive bias in the deep-tropical latitudes and negative bias in higher latitudes in both hemispheres (Fig. 10d).

Figure 10e and f show the sub-ensemble averaged CMIP5-to-CMIP6  $\|STF\|_L$  change of the six TOP10 models with negative CMIP5-to-CMIP6 changes in  $\|AET_{EQ}\|$  and SYM-PC. In the NH, the bias over the subtropics and extra-tropical regions is largely alleviated. In the high-latitude North Pacific Ocean (ocean area within the box  $20^\circ N \sim 60^\circ N$ ,  $120^\circ E \sim 90^\circ W$ ), the bias in roughly 75% of the area is reduced from CMIP5 to CMIP6 (Fig. 10e). Additionally, the zonal dipole bias in the North Atlantic is significantly reduced in CMIP6. In the Southern Hemisphere, there is an increase in negative bias over the deep-tropical ocean area and a substantial decrease in positive bias in the subtropical and extratropical areas (Fig. 10e). In more than 77% of the subtropical and extra-tropical regions ( $20^\circ S \sim 70^\circ S$ ), the sub-ensemble mean bias in CMIP5 displays reduction in CMIP6. For the zonal integral of  $\|STF\|_L$ , the subtropical and extra-tropical negative bias of the six selected CMIP5 models is systematically reduced in CMIP6. While, the negative bias in the deep-tropics of SH is enhanced in CMIP6.

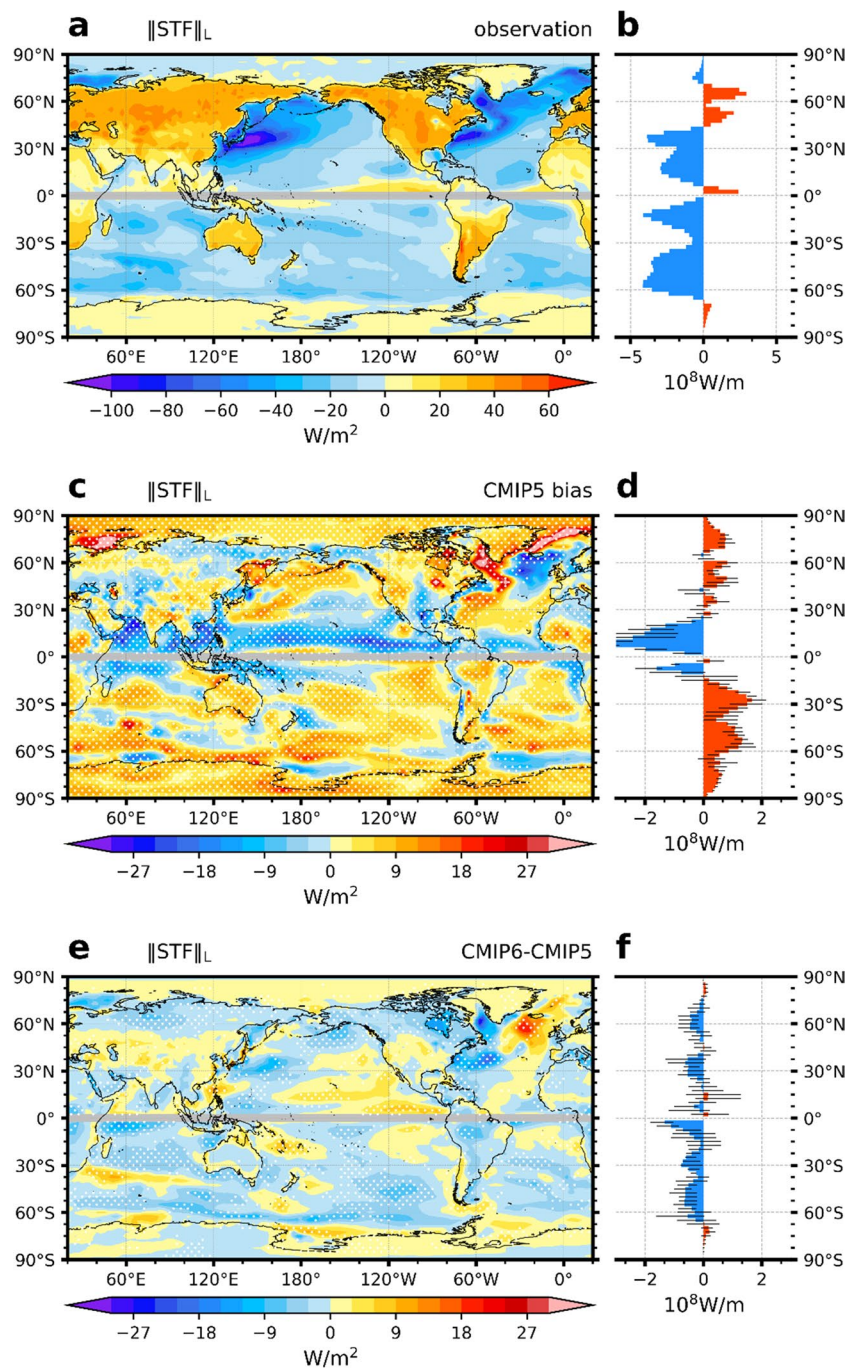
In summary, the observed local seasonal contrast of  $STF$  is better reproduced by the six TOP10 models, which feature negative CMIP5-to-CMIP6 changes in  $\|AET_{EQ}\|$  and SYM-PC, in CMIP6 than their counterparts in CMIP5. The decrease of the subtropical and extra-tropical positive bias in  $\|STF\|_L$  and the increase of the negative bias in deep-tropics collectively contribute to the decrease in the seasonal contrast of the hemispheric contrast of surface turbulent flux ( $\|STF\|$ ).

## 4 Summary and concluding remarks

### 4.1 Summary

In this study, we applied the EOF analysis to the symmetric and antisymmetric components of the zonal mean precipitation biases of the CMIP6 and CMIP6 models, and extracted the leading modes of the symmetric and antisymmetric biases in the zonal mean tropical precipitation. On the basis of these two EOF modes, we quantified the improvement in the simulation of tropical precipitation from CMIP5 to CMIP6, and highlighted the remarkable progresses in ten model pairs. In addition, we further investigated the linkage between the changes of precipitation and the changes in the cross-equatorial atmospheric energy transport ( $AET_{EQ}$ ), and diagnosed the biases in the hemispheric energy budget

**Fig. 10** **a** Spatial distribution of local seasonal contrast of  $STF$  ( $\|STF\|_L$ ) inferred from CERES radiative fluxes and mass-corrected ERA5 total atmospheric energy divergence and tendency. **b** the distance-weighted zonal integral of (a). **c, d** same as (a, b), but for the bias of the six TOP10 model pairs with negative CMIP5-to-CMIP6 changes in the SYM-PC and the  $\|AET_{EQ}\|$ . Stippling in (c) denote the area where at least five of the six models agree on the sign of biases. The inter-quartile range of the percentiles of the selected CMIP5 models are denoted by error bars in (d). **e, f** same as (c, d), but for the difference between CMIP6 and CMIP5

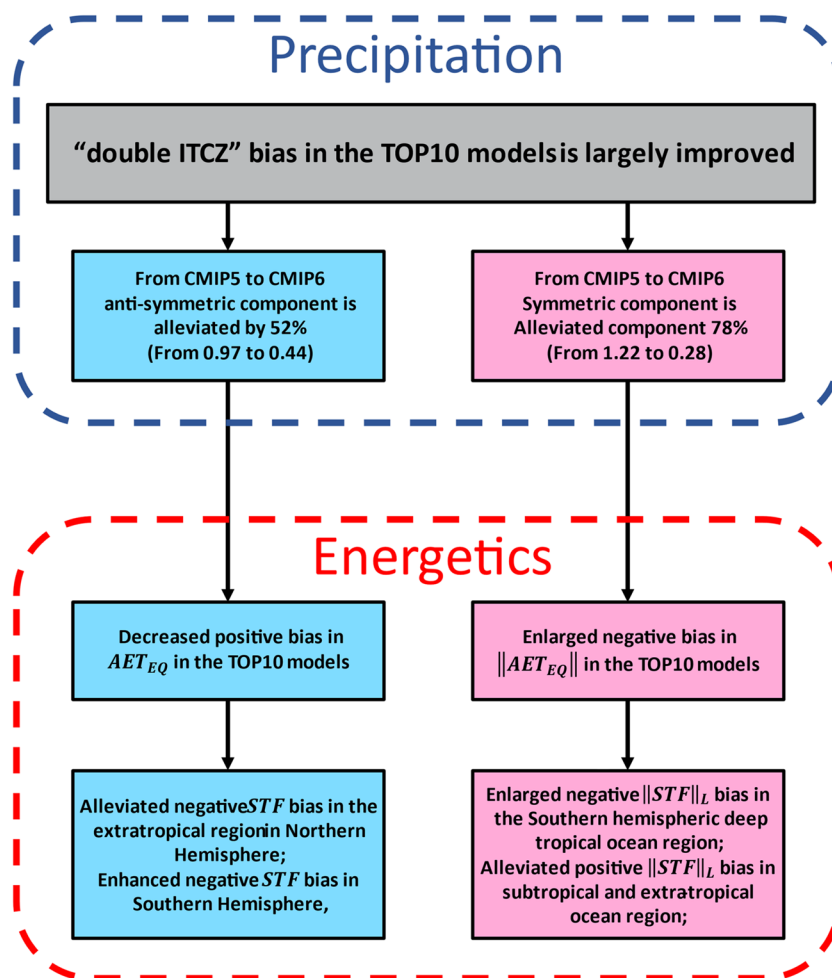


for the models with significantly improved simulations of tropical precipitation in CMIP6. The main conclusions are summarized below, and briefly expressed in Fig. 11:

- (1) The CMIP6 models shows improvement in the simulation of tropical precipitation than those in CMIP5. Dividing these model pairs into two sub-ensembles by the CMIP5-to-CMIP6 changes of RMSE, we found significant improvement happens in the top ten models (TOP10) with larger reduction in the RMSE. In

contrast, the bottom ten models (BOT10) with smaller RMSE reduction exhibit a similar bias pattern between CMIP5 and CMIP6. Further EOF analysis shows that the anti-symmetric component of the TOP10 mean is alleviated by 52% (From 0.97 to 0.44) from CMIP5 to CMIP6, while its symmetric component is reduced by 78% (From 1.22 to 0.28). In contrast, the BOT10 mean bias in CMIP5 generally persists in CMIP6. These results indicate that the persistent anti-symmetric and symmetric tropical precipitation biases in a subset of

**Fig. 11** Brief conclusions of this study. The improvement in the antisymmetric and symmetric components of the tropical precipitation bias from CMIP5 to CMIP6 is linked to the changes in the atmospheric energy balance



CMIP5 models have been largely alleviated in CMIP6. Detailed analysis on these improved models is needed so as to advance our physical understanding of the “double-ITCZ” bias.

- (2) The anti-symmetric mode of the “double ITCZ” bias is significantly correlated with the annual mean  $AET_{EQ}$ . The decrease of ASYM-PC from CMIP5 to CMIP6 is usually accompanied with the increase of  $AET_{EQ}$ . Diagnosis of the interhemispheric energy balance budget for the six TOP10 model pairs with negative CMIP5-to-CMIP6 changes in the ASYM-PC and positive changes in the  $AET_{EQ}$  shows that the mean increase in  $AET_{EQ}$  (0.21 PW) of these model pairs mainly stems from the reduction of the negative  $[STF]$  bias (0.12 PW). The reduction in the  $[STF]$  bias is mainly contributed by a reduction (increase) in the negative  $STF$  bias in the extratropical region of the NH (SH). The increased heating in North Atlantic Ocean and decreased heating in Southern Ocean contribute significantly to the decrease in  $[STF]$ .
- (3) The symmetric mode of the “double ITCZ” bias is significantly correlated with the seasonal contrast of

$AET_{EQ}$  ( $\|AET_{EQ}\|$ ). In TOP10, there are six models showing decrease in SYM-PC and enlargement in the negative bias of  $\|AET_{EQ}\|$  from CMIP5 to CMIP6. Further budget analysis shows that the negative changes in the  $\|AET_{EQ}\|$  from CMIP5 to CMIP6 is dominated by the decrease in seasonal contrast of the hemispheric contrast in surface turbulent flux ( $\|[STF]\|$ ). The spatial pattern of  $\|STF\|_L$  reveals a reduction of the positive bias in subtropical and extra-tropical regions, alongside an increase of negative bias in deep-tropical regions. These combined factors lead to the CMIP5-to-CMIP6 reduction in positive  $\|[STF]\|$  bias.

## 4.2 Discussion

In this study, the observation of surface turbulent flux is derived from a residual method (Loeb et al. 2022; Trenberth et al. 2019). The surface flux product estimated by bulk flux algorithms, such as OaFlux (Yu and Weller 2007), are not used in our study, as these direct estimations still have some evident issues such as: uncertainties in the near-surface



meteorological variables and the formulation of bulk flux parameterizations (Li et al. 2015a; Yu 2019).

The atmospheric energetics analyses in this work could not demonstrate the causals of the “double ITCZ” problem, because the circulation, cloud, and SST are coupled with each other and may all contribute to the budget of the hemispheric energy balance. However, our analyses provided an energetics perspective to constrain the simulation of tropical precipitation. The framework of hemispheric energy balance (Loeb et al. 2016), enable us to identify whether the improvements in the simulation of tropical precipitation are related to some solid progresses in the representation of atmospheric energy balance or due to some wrong reason, such as the cancellation between the biases of different atmospheric heating processes. In addition, it also supplies an approach to test some existing mechanisms.

The mechanisms that are reported to cause the antisymmetric “double ITCZ” biases could be concluded as two groups. One claims that the heating bias in the extra-tropical region could propagate to the tropics and lead to the “double ITCZ” bias (Hwang and Frierson 2013; Kawai et al. 2021; Lee et al. 2022; Li and Xie 2014; Mechoso et al. 2016). the other emphasize the intra-tropical source causing the antisymmetric biases (Baldwin et al. 2021; Gonzalez et al. 2024; Liu et al. 2023; Xiang et al. 2017; Zhou et al. 2022). Our analysis here shows that, over the subtropical and extratropical region the negative *STF* bias is stronger in the Southern Hemisphere than that in the Northern Hemisphere for a sub-ensemble of CMIP5 models (Fig. 7c). These results fit well with the hypothesis that the extra-tropical heating bias could partly contribute to the tropical precipitation bias. In the CMIP6, this extra-tropical *STF* bias is alleviated. correspondingly, the anti-symmetric “double ITCZ” get partly eliminated. Therefore, we suppose that it is the change of *STF* in the extra-tropical regions that lead to the alleviation of the antisymmetric mode in CMIP6.

The annual cycle of cross-equatorial atmospheric energy transport (Donohoe et al. 2019; Kim et al. 2021) and equatorial Pacific cold tongue (Kim et al. 2021; Li and Xie 2014; Ma et al. 2023; Wang et al. 2020) are pointed out as two important elements causing the symmetric “double ITCZ” bias. According to the interhemispheric energy budget, the cross-equatorial atmospheric energy transport is linked to the hemispheric contrast of the atmospheric heating (Kim et al. 2021). Based on an inter-model correlation approach, previous work deduce that the short shortwave radiation absorbed in the atmosphere (*SWA*) is the key element leading to the biases in the annual cycle of cross-equatorial atmospheric energy transport (Kim et al. 2021). However, our quantitative evaluation based on the atmospheric energy balance shows that the biases in the surface turbulent energy flux (*STF*) is also important and even contribute more to  $AET_{EQ}$  bias in the TOP10 of CMIP5 models. In addition, we

noted that the linear regression lines in the Fig. 8c and b do not pass through the origin of coordinate, which indicates that the  $\|AET_{EQ}\|$  is not the only element contributing to the symmetric “double ITCZ” bias in CMIP5 and CMIP6. Considering the “cold tongue” bias is the other element causing the symmetric “double ITCZ” (Kim et al. 2021; Li and Xie 2014). The enlarged biases in  $\|AET_{EQ}\|$  may compensate the influence of “cold tongue” biases in the TOP10 models of CMIP6, and alleviate the symmetric “double ITCZ”.

**Acknowledgements** This work is jointly supported by the National Natural Science Foundation of China (Grant No. 41988101) and the Second Tibetan Plateau Scientific Expedition and Research (STEP) program (Grant No.2019QZKK0102). We are grateful to Dr. Bo Wu, Dr. Xiaolong Chen, and Dr. Lixia Zhang for their helpful suggestions in the panel discussion.

**Author’s contributions** All authors contributed to the study conception and design.. The first draft of the manuscript was written by Zikun Ren. All authors read and approved the final manuscript.”

**Funding** This work is jointly supported by the National Natural Science Foundation of China (Grant No. 41988101) and the Second Tibetan Plateau Scientific Expedition and Research (STEP) program (Grant No.2019QZKK0102).

**Data availability** All datasets used in this study are freely available for download by the following links: CERES EBAF TOA Edition 4.1 Data Product: [https://doi.org/10.5067/TERRA-AQUA/CERES/EBAF-TOA\\_L3B004.1](https://doi.org/10.5067/TERRA-AQUA/CERES/EBAF-TOA_L3B004.1). CERES EBAF Surface Edition 4.1 Data Product: [https://doi.org/10.5067/Terra-Aqua/CERES/EBAF\\_L3B.004.1](https://doi.org/10.5067/Terra-Aqua/CERES/EBAF_L3B.004.1). mass corrected vertically integrated energy budget terms for ERA5: <https://cds.climate.copernicus.eu/cdsapp/dataset/derived-reanalysis-energy-moisture-budget>. Global Precipitation Climatology Project (GPCP v2.3): <https://psl.noaa.gov/data/gridded/data.gpcp.html>. Climate Prediction Center (CPC) Merged Analysis of Precipitation (CMAP v1201): <https://psl.noaa.gov/data/gridded/data.cmap.html>. CMIP6 historical simulations: <https://esgf-node.llnl.gov/search/cmip6/>. CMIP5 historical simulations: <https://esgf-node.llnl.gov/search/cmip5/>.

**Code availability** All relevant codes used in this work are available, upon request, from the corresponding author T.Z.

## Declarations

**Competing interests** The authors declare no competing interests.

**Open Access** This article is licensed under a Creative Commons Attribution 4.0 International License, which permits use, sharing, adaptation, distribution and reproduction in any medium or format, as long as you give appropriate credit to the original author(s) and the source, provide a link to the Creative Commons licence, and indicate if changes were made. The images or other third party material in this article are included in the article’s Creative Commons licence, unless indicated otherwise in a credit line to the material. If material is not included in the article’s Creative Commons licence and your intended use is not permitted by statutory regulation or exceeds the permitted use, you will need to obtain permission directly from the copyright holder. To view a copy of this licence, visit <http://creativecommons.org/licenses/by/4.0/>.



## References

- Adam O, Schneider T, Brient F, Bischoff T (2016) Relation of the double-ITCZ bias to the atmospheric energy budget in climate models. *Geophys Res Lett* 43:7670–7677
- Adler RF, Huffman GJ, Chang A, Ferraro R, Xie PP, Janowiak J, Rudolf B, Schneider U, Curtis S, Bolvin D, Gruber A, Susskind J, Arkin P, Nelkin E (2003) The version-2 global precipitation climatology project (GPCP) monthly precipitation analysis (1979–present). *J Hydrometeorol* 4:1147–1167
- Baldwin JW, Atwood AR, Vecchi GA, Battisti DS (2021) Outsize influence of central American orography on global climate. *AGU Adv*:2
- Bellucci A, Gualdi S, Navarra A (2010) The double-ITCZ syndrome in coupled general circulation models: the role of large-scale vertical circulation regimes. *J Clim* 23:1127–1145
- Bischoff T, Schneider T (2016) The equatorial energy balance, ITCZ position, and double-ITCZ bifurcations. *J Clim* 29:2997–3013
- Donohoe A, Atwood AR, Byrne MP (2019) Controls on the width of tropical precipitation and its contraction under global warming. *Geophys Res Lett* 46:9958–9967
- Donohoe A, Marshall J, Ferreira D, McGee D (2013) The relationship between ITCZ location and cross-equatorial atmospheric heat transport: from the seasonal cycle to the last glacial maximum. *J Clim* 26:3597–3618
- Eyring V, Bony S, Meehl GA, Senior CA, Stevens B, Stouffer RJ, Taylor KE (2016) Overview of the coupled model Intercomparison project phase 6 (CMIP6) experimental design and organization. *Geosci Model Dev* 9:1937–1958
- Frierson DMW, Hwang YT (2012) Extratropical influence on ITCZ shifts in Slab Ocean simulations of global warming. *J Clim* 25:720–733
- Frierson DMW, Hwang Y-T, Fučkar N et al (2013) Contribution of ocean overturning circulation to tropical rainfall peak in the Northern Hemisphere. *Nature Geosci* 6:940–944
- Fushan D, Rucong Y, Xuehong Z et al (2005) Impacts of an improved low-level cloud scheme on the eastern Pacific ITCZ-cold tongue complex. *Adv Atmos Sci* 22:559–574
- Gonzalez AO, Ganguly I, Osterloh M, Cesana GV, Demott CA (2024) Dynamical importance of the trade wind inversion in suppressing the Southeast Pacific ITCZ. *J Geophys Res-Atmos* 129:e2023JD039571
- Hersbach H, Bell B, Berrisford P, Hirahara S, Horanyi A, Muñoz-Sabater J, Nicolas J, Peubey C, Radu R, Schepers D, Simmons A, Soci C, Abdalla S, Abellan X, Balsamo G, Bechtold P, Biavati G, Bidlot J, Bonavita M, Thépaut JN (2020) The ERA5 global reanalysis. *Q J R Meteorol Soc* 146:1999–2049
- Hwang Y-T, Frierson DMW (2013) Link between the double-intertropical convergence zone problem and cloud biases over the Southern Ocean. *Proc Natl Acad Sci USA* 110:4935–4940
- Jones PW (1999) First- and second-order conservative remapping schemes for grids in spherical coordinates. *Mon Weather Rev* 127:2204–2210
- Kato S, Rose FG, Rutan DA, Thorsen TJ, Loeb NG, Doelling DR, Huang X, Smith WL, Su W, Ham S-H (2018) Surface irradiances of edition 4.0 clouds and the Earth's radiant energy system (CERES) energy balanced and filled (EBAF) data product. *J Clim* 31:4501–4527
- Kawai H, Koshiro T, Yukimoto S (2021) Relationship between short-wave radiation bias over the Southern Ocean and the double-intertropical convergence zone problem in MRI-ESM 2. *Atmos Sci Lett* 22(12):e1064
- Kim H, Kang SM, Takahashi K, Donohoe A, Pendergrass AG (2021) Mechanisms of tropical precipitation biases in climate models. *Clim Dyn* 56:17–27
- Lee J, Kang SM, Kim H, Xiang BQ (2022) Disentangling the effect of regional SST bias on the double-ITCZ problem. *Clim Dyn* 58:3441–3453
- Li G, Du Y, Xu HM, Ren BH (2015a) An intermodel approach to identify the source of excessive equatorial Pacific cold tongue in CMIP5 models and uncertainty in observational datasets. *J Clim* 28:7630–7640
- Li G, Xie S-P (2014) Tropical biases in CMIP5 multimodel ensemble: the excessive equatorial Pacific cold tongue and double ITCZ problems. *J Clim* 27:1765–1780
- Li G, Xie SP (2012) Origins of tropical-wide SST biases in CMIP multi-model ensembles. *Geophys Res Lett* 39:L22703
- Li G, Xie SP, Du Y (2015b) Monsoon-induced biases of climate models over the tropical Indian Ocean. *J Clim* 28:3058–3072
- Liu CL, Chen N, Long JC, Cao N, Liao XQ, Yang YZ, Ou NS, Jin L, Zheng R, Yang K, Su QY (2022) Review of the observed energy flow in the earth system. *Atmosphere* 13:10
- Liu T, Liu Z, Zhao Y, Zhang S (2023) Subtropical impact on the tropical double-ITCZ Bias in the GFDL CM2.1 model. *J Clim* 36:3833–3847
- Lin JL (2007) The double-ITCZ problem in IPCC AR4 coupled GCMs: ocean-atmosphere feedback analysis. *J Clim* 20:4497–4525
- Loeb NG, Doelling DR, Wang H, Su W, Nguyen C, Corbett JG, Liang L, Mitrescu C, Rose FG, Kato S (2018) Clouds and the Earth's radiant energy system (CERES) energy balanced and filled (EBAF) top-of-atmosphere (TOA) Edition-4.0 data product. *J Clim* 31:895–918
- Loeb NG, Mayer M, Kato S, Fasullo JT, Zuo H, Senan R, Lyman JM, Johnson GC, Balmaseda M (2022) Evaluating twenty-year trends in Earth's energy flows from observations and Reanalyses. *J Geophys Res-Atmos* 127:e2022JD036686
- Loeb NG, Wang H, Cheng A, Kato S, Fasullo JT, Xu K-M, Allan RP (2016) Observational constraints on atmospheric and oceanic cross-equatorial heat transports: revisiting the precipitation asymmetry problem in climate models. *Clim Dyn* 46:3239–3257
- Ma XY, Zhao SY, Zhang H, Wang WK (2023) The double-ITCZ problem in CMIP6 and the influences of deep convection and model resolution. *Int J Climatol* 43(5):2369–2390
- Mayer J, Mayer M, Haimberger L (2021) Consistency and homogeneity of atmospheric energy, moisture, and mass budgets in ERA5. *J Clim* 34:3955–3974
- Mechoso CR, Losada T, Koseki S, Mohino-Harris E, Keenlyside N, Castano-Tierno A, Myers TA, Rodriguez-Fonseca B, Toniazzo T (2016) Can reducing the incoming energy flux over the Southern Ocean in a CGCM improve its simulation of tropical climate? *Geophys Res Lett* 43:11057–11063
- Peixoto JP, Oort AH (1992) *Physics of climate*. American Institute of Physics, Melville, NY
- Si W, Liu H, Zhang X, Zhang M (2021) Double intertropical convergence zones in coupled ocean-atmosphere models: Progress in CMIP6. *Geophys Res Lett* 48:e2021GL094779
- Song F, Zhang GJ (2016). Effects of southeastern Pacific sea surface temperature on the double-ITCZ bias in NCAR CESM1. *Journal of Climate* 29(20):7417–7433.
- Taylor KE, Stouffer RJ, Meehl GA (2012) An OVERVIEW of CMIP5 and the experiment design. *Bull Am Meteorol Soc* 93:485–498
- Tian BJ, Dong XY (2020) The double-ITCZ Bias in CMIP3, CMIP5, and CMIP6 models based on annual mean precipitation. *Geophys Res Lett* 47:11
- Trenberth KE, Zhang Y, Fasullo JT, Cheng L (2019) Observation-based estimates of global and Basin Ocean meridional heat transport time series. *J Clim* 32:4567–4584
- Wang CG, Hu YY, Wen XY, Zhou C, Liu JP (2020) Inter-model spread of the climatological annual mean Hadley circulation and its relationship with the double ITCZ bias in CMIP5. *Clim Dyn* 55:2823–2834

- Wielicki BA, Barkstrom BR, Harrison EF, Lee RB, Smith GL, Cooper JE (1996) Clouds and the earth's radiant energy system (CERES): an earth observing system experiment. *Bull Am Meteorol Soc* 77:853–868
- Xiang BQ, Zhao M, Held IM, Golaz JC (2017) Predicting the severity of spurious "double ITCZ" problem in CMIP5 coupled models from AMIP simulations. *Geophys Res Lett* 44:1520–1527
- Xie PP, Arkin PA (1997) Global precipitation: a 17-year monthly analysis based on gauge observations, satellite estimates, and numerical model outputs. *Bull Am Meteorol Soc* 78:2539–2558
- Yu L (2019) Global air–sea fluxes of heat, fresh water, and momentum: energy budget closure and unanswered questions. *Ann Rev Mar Sci* 11:227–248
- Yu L, Weller RA (2007) Objectively analyzed air-sea heat fluxes for the global ice-free oceans (1981–2005). *Bull Am Meteorol Soc* 88:527–+
- Zhang GJ, Wang HJ (2006) Toward mitigating the double ITCZ problem in NCAR CCSM3. *Geophys Res Lett* 33:L06709
- Zhou WY, Leung LR, Lu J (2022) Linking large-scale double-ITCZ Bias to local-scale drizzling Bias in climate models. *J Clim* 35:4365–4379
- Zhou WY, Xie SP (2017) Intermodel spread of the double-ITCZ bias in coupled GCMs tied to land surface temperature in AMIP GCMs. *Geophys Res Lett* 44:7975–7984

**Publisher's Note** Springer Nature remains neutral with regard to jurisdictional claims in published maps and institutional affiliations.